ISSN 0503-1540

Tome 19 *Novembre 1981* Numéro 4

La mer

うみ

昭和 56 年 11 月

日 仏 海 洋 学 会

La Société franco-japonaise
d'océanographie
Tokyo, Japon

日仏海洋学会

編集委員会

投稿規定

1. 報文の投稿者は本会会員に限る。
2. 原稿は簡潔にわかりやすく書き，図表を含めて印刷ページで**10ページ以内**を原則とする。原稿（**正1通，副1通**）は，（〒101）東京都千代田区神田駿河台2-3　日仏会館内　日仏海洋学会編集委員会宛に送ること。
3. 編集委員会は，事情により原稿の字句の加除訂正を行うことがある。
4. 論文（欧文，和文とも）には必ず約200語の欧文（原則として仏語）の要旨をつけること。欧文論文には欧文の要旨のほかに必ず約500字の和文の要旨をつけること。
5. 図及び表は必要なもののみに限る。図はそのまま版下になるように縮尺を考慮して鮮明に黒インクで書き，論文の図及び表には必ず英文（又は仏文）の説明をつけること。
6. 初校は原則として著者が行う。
7. 報文には1編につき50部の別刷を無料で著者に進呈する。これ以上の部数に対しては，実費（送料を含む）を著者が負担する。

RECOMMANDATIONS A L'USAGE DES AUTEURS

1. Les auteurs doivent être des membres de la Société franco-japonaise d'océanographie.
2. Les notes ne peuvent dépasser dix pages. Les manuscrits à deux exemplaires, dactylographiés sur papier fort, doivent être envoyés au Comité de rédaction de la Société franco-japonaise d'océanographie, c/o Maison franco-japonaise, 2-3, Kanda Surugadai, Chiyoda-ku, Tokyo, 101 Japon.
3. Le Comité de rédaction se réserve le droit d'apporter, le cas échéant, des modifications mineuses aux manuscrits ainsi que de demander aux auteurs de les corriger.
4. Des résumés en langue japonaise ou langue française sont obligatoires.
5. Les figures au trait seront tracées à l'encre de Chine noire sur papier blanc ou sur calque. Les légendes des figures et des tableaux sont indispensables.
6. Les premières épreuves seront corrigées, en principe, par les auteurs.
7. Un tirage à part des articles en cinquante exemplaires est offert gratuitement aux auteurs. Ceux qui en désirent un plus grand nombre peuvent les faire établir à leurs frais.

La mer 19: 159-164, 1981
Société franco-japonaise d'océanographie, Tokyo

Relationship between Turbidity of Water and Visual Acuity of Fish (1)*

Kanau MATSUIKE**, Yoshikazu SHIMAZU** and Yoshihiko NAKAMURA**

Abstract: The relationship between turbidity of water and visual acuity of fish was examined by means of the conditioned reflex method. Carp (*Cyprinus carpio*) were selected as experimental fish. The visual acuities under reasonable brightness conditions are estimated to be 0.106 in clear water, 0.097 in turbid water of 1 ppm (beam attenuation coefficient, 1.25 m^{-1}), 0.090 in 2 ppm (2.50 m^{-1}), and 0.065 in 3 ppm (3.75 m^{-1}). Subsequently, concerning the decrease of visual acuity of fish in turbid water, the apparent contrast and the masking phenomenon of target by suspended particles were discussed. The lowering of visual acuities in turbid water of less than 2 ppm is explained by the masking phenomenon; however, in turbid water of more than 2 ppm it is influenced by the decrease in apparent contrast in addition to the masking phenomenon.

1. Introduction

Turbidity of water reduces the transmittance of light and decreases the contrast between objects and their surrounding background. Therefore, it is considered to exert influence on the visual acuity of fish.

In respect to the studies of visual acuity in fish, much research was carried out on the physiological aspect of the retina (KAHMANN, 1934, 1936; TAMURA, 1957; TAMURA and WISBY, 1963; O'CONNELL, 1963; KAWAMURA and TAMURA, 1973), but others were from an ecological standpoint (BRUNNER, 1934; YAMANOUCHI, 1956; NAKAMURA, 1968; HESTER, 1968). BRUNNER (1934) and YAMANOUCHI (1956) examined European minnow (*Phoxinus laevis*) and convictfish (*Microcanthus strigatus*) by means of the conditioned reflex method and found their visual acuities to be 0.09 and 0.2. NAKAMURA (1968) also studied the influence of brightness to visual acuity using skipjack tuna (*Katsuwonus pelamis*) and little tunny (*Euthynnus affinis*), and concluded the visual acuities of them to be 0.180 and 0.135. HESTER (1968) studied goldfish (*Carassius auratus*) to find the relation of target diameter to contrast thresholds at each of four levels of adaptive radiance.

All of the efforts mentioned above were to find the visual acuities of fish in clear and transparent water. However, we cannot find any studies that clarify the decrease in visual acuities of fish in relation to different water turbidity, which is, in fact, one of the significant factors in evaluating fishing gear and method.

In this study, carp (*Cyprinus carpio*) were selected as experimental fish and the relationship between turbidity of water and their visual acuity was examined by means of the conditioned reflex method.

(Note) Visual acuity — the reciprocal of the visual angle (minutes of arc) made at the position of the eye, when the smallest physical solid at a certain distance apart from the eye is seen — is generally concerned with the ideal conditions of clear water; however, the term "visual acuity" is also used in this study for turbid water.

2. Methods

Experimental fish

Three one-year old carp (*Cyprinus carpio*) of different body lengths (8, 11 and 12 cm) were used.

Experimental tank

An outlined construction of the experimental tank is shown in Fig. 1. The rear part of the tank is divided into two compartments by a

* Received June 20, 1981
Partly presented at the Annual Meeting of the Society, May 1980
** Tokyo University of Fisheries, Konan 4-5-7, Minato-ku, Tokyo, 108 Japan

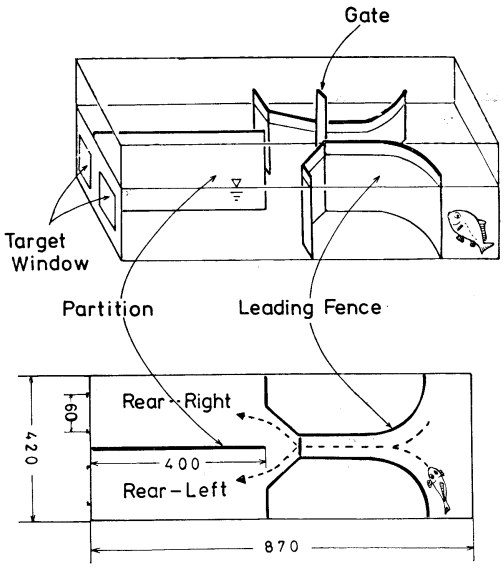

Fig. 1. Experimental tank.

Table 1. Apparent contrast in clear and turbid water.

	Clear water	Turbid water		
		1 ppm	2 ppm	3 ppm
Apparent contrast	16.6	2.46	1.05	0.70

partition 400 mm long, and the end wall of each compartment contains a square target window at its center. The observation window is positioned in the upper part of the end wall. There is a pair of leading fences and a gate which is about 140 mm from the front edge of the partition. All of the wall surfaces, except the target and observation windows, are covered with white acrylic resin board. A light source located above the tank is arranged so that the tank is illuminated evenly. The underwater brightness at the inside surface of the target window was 480 lux in clear water and 430 lux in turbid water of 3 ppm.

The target board was made of white acrylic resin with a black square in the center. A side of the square was 1, 2, 3, 4 or 5 mm.

The apparent contrast, $C_{(r)}$, is calculated using the following formula:

$$C_{(r)}=\frac{B_{t(r)}-B_{b(r)}}{B_{b(r)}},$$

where $B_{t(r)}$ is apparent target radiance of the white part and $B_{b(r)}$ is that of the black part at a distance r from the target. The apparent contrast in water at a distance of 400 mm from the target is shown in Table 1. The apparent target radiances were measured by a Topcon luminance meter (Model BM-3).

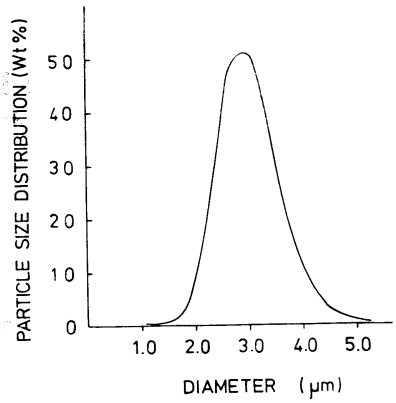

Fig. 2. Particle size distribution of *Chlorella ellipsoidea* used.

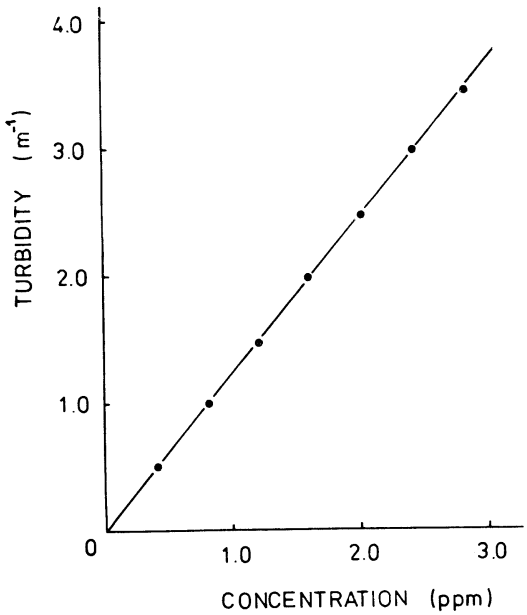

Fig. 3. Relationship between *Chlorella* concentration (ppm) and beam attenuation coefficient (m^{-1}; wavelength of gravity center, 486 nm).

Cultured *Chlorella ellipsoidea* accounted for the turbidity of the experimental water. The size distribution of this alga is shown in Fig. 2. The mean value is 3.0 μm in diameter. The

beam transmittances of the turbid water were measured by an EMS transmissometer (Martek) with a blue filter (wavelength of gravity center, 486 mm). The relationship between *Chlorella* concentration (ppm) and beam attenuation coefficient is illustrated in Fig. 3.

Training of fish

Three carp were trained individually in the following manner:

1) A white acrylic resin board was attached to one of the target windows and a target board was attached to the other window.
2) A carp was released into the front compartment.
3) By opening the gate, the fish proceeded to one of the two rear compartments. If the fish reached the compartment which contained the target board, the fish was given a piece of food (pellet No. 8) as a reward.
4) The fish was moved back to the front compartment and the gate was closed.
5) The above procedures were repeated by changing, at random, the target board right to left or vice versa.

The experiments were conducted 5–10 times a day and about 300 times in total. In this manner, the preliminary experiment was completed, and the rate of "correct behaviors" (target recognition) at this stage was found to be more than 80 %.

Subsequently, each fish was re-trained as the size of the target was reduced step by step, because the rate of "correct behaviors" decreased distinctly each time the target size was reduced. Such experiments were carried out about 450 times, and the rate of "correct behaviors" at this stage was also more than 80 %.

Main experiment

Firstly, a series of experiments were conducted using three well-trained fish one at a time. Each fish was examined in clear water to find the rate of "correct behaviors" by changing the target size. These experiments were conducted 30 times for each fish.

Secondly, the same experiments as mentioned above were carried out in turbid water of 1, 2 and 3 ppm. The experiments were carried out 30 times for each fish.

3. Results and discussions

Fig. 4 shows the rate of "correct behaviors" after changing the target size in clear water. The solid circle in the graph shows the mean value of three individual fish. The rate of "correct behaviors" is more than 90 % for target sizes of 5 and 4 mm, and more than 80 % for 3 and 2 mm, but the rate abruptly decreases for 1 mm. The carp's threshold of discrimination, therefore, is estimated to be between 1 and 2 mm. The rate of "correct behaviors" at this threshold is deduced to be 63 % by statistic analysis (binominal distribution at 1 % significance level), and the size of the target based on the threshold of discrimination corresponds to 1.1 mm in length. As a result, the visual acuity of carp in clear water is estimated to be 0.106.

Fig. 5 shows the rate of "correct behaviors" for each of the different target sizes after changing the turbidity. The graph clearly illustrates that the more turbid the water is, the larger the visual angle (the smaller the visual acuity) of carp. In order for this aspect to be more

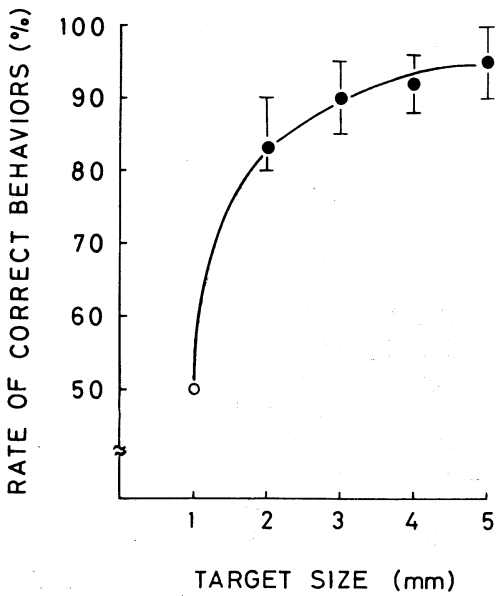

Fig. 4. The rate of "correct behaviors" for different target sizes in clear water. Solid circle indicates the mean values of three individual fish. The open circle illustrates the rates of less than 50 %.

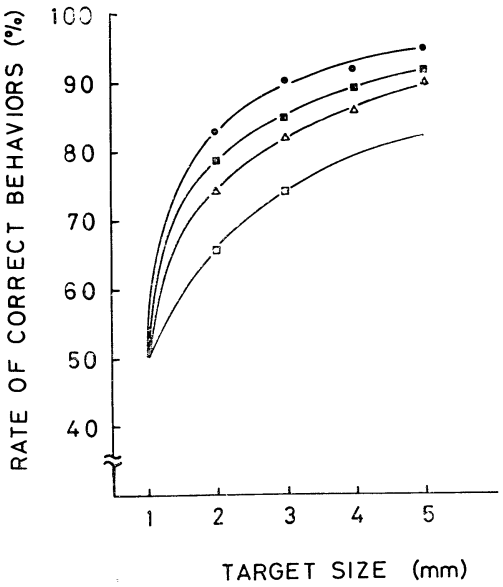

Fig. 5. The rate of "correct behaviors" for different target sizes after changing the turbidity. Symbols ●, ■, △ and □ stand for the mean value in clear water and turbid water of 1, 2 and 3 ppm, respectively.

Table 2. Relationship between turbidity and visual acuity.

Turbidity (ppm)	Bean attenuation coefficient (m^{-1})	Visual acuity	Visual angle (min. of arc)
1	1.25	0.097	10.31
2	2.50	0.090	11.17
3	3.75	0.065	15.47

easily understood, the relationship between turbidity and visual acuity at a rate of "correct behaviors" of 63% is shown in Table 2. The visual acuity of carp (0.106 in clear water) scarcely changes even in turbid water with beam attenuation coefficient of less than 1.3 m^{-1}, but it decreases greatly in more turbid water.

The decrease in the visual acuity of fish in turbid water is generally caused by the lowering of brightness and object contrast. In addition, however, it may also be expected that the masking phenomenon of the target within the visual angle caused by suspended particles is of importance, especially in experiments of visual acuity which use a small target as in the present paper. In order to determine the most

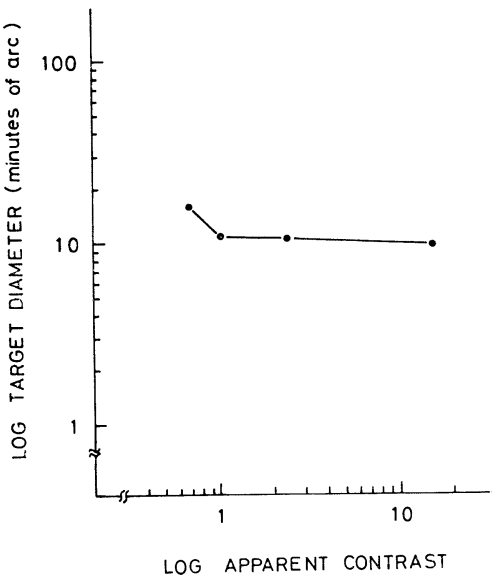

Fig. 6. Relationship between target diameter at the limit of discrimination and apparent contrast.

influential factor on the decrease in visual acuity of fish in turbid water, each of the factors involved is examined separately based on the results of the present experiments.

Underwater brightness

NAKAMURA (1968) conducted research into the relationship between visual acuity and brightness in skipjack tuna and little tunny in clear water. According to his result, there is no influence of the brightness on visual acuity under brightness of 170 lux. In the most turbid water of 3 ppm used in the present experiment the brightness was 430 lux. This value is considerably high as compared with the critical limit of the brightness achieved by NAKAMURA (1968) for the influence on visual acuity. Therefore, it may be concluded that the brightness is not a factor in the decrease of visual acuity in the turbid water concerned.

Apparent contrast

The relationship between apparent contrast and target size at the limit of discrimination is shown in Fig. 6. The target size at the limit of discrimination hardly changes with an increase of the apparent contrast of more than 1.1, whereas it suddenly becomes larger with a decrease of the apparent contrast of less than

1.1. Namely, in decreasing the contrast value, the increase in target size is required to be visible. This tendency highly resembles the results of HESTER (1968).

From the fact that the critical target size hardly changes with an increase in the apparent contrast of more than 1.1, it can be said at least that the decrease in the apparent contrast in turbid water of less than 2 ppm is not a cause in the decrease of visual acuity.

Masking phenomenon of target in suspended particles

In turbid water, the target as seen with the fish eye from a certain distance is masked by the suspended particles existing in the visual angle. In the case of a target of diameter D seen from distance L, the area dA masked by the particles of minute volume existing at x from the eye is expressed as follows:

$$dA=\left(\frac{\pi}{4}\right)^2 SD^2\phi^2 dx\,, \qquad (1)$$

where ϕ is the mean particle diameter, and S the number of particles per unit volume. In a different expression, the increased area dB of target is shown as follows:

$$dB=\frac{\pi}{2}D\,dD\,. \qquad (2)$$

The target area at the limit of discrimination in turbid water is taken to be the sum of the area discernible in clear water and the area masked by suspended particles. Therefore, the target size when dA is equal to dB is the limit of discrimination, and the target diameter D at that time is expressed as follows:

$$D=\exp\left(\frac{\pi}{8}S\phi^2 L+C\right), \qquad (3)$$

where C is a constant.

By substitution in equation (3) of $S=70/\text{mm}^3$, $\phi=3.0\times10^{-3}$, $L=400$ mm, and $C=9.531\times10^{-2}$ as calculated in clear water where $D=1.1$ mm and $S=0/\text{mm}^3$, the target diameters at the limit of discrimination in different turbid water are obtained as shown in Table 3. When these theoretical values are compared with the experimental values, they coincide quite well with each other in the range of turbidity lower than 2 ppm. However, for turbidity higher than 2 ppm the experimental values become larger than the theoretical ones (Fig. 7). This is thought to be caused by the additional influence of the decrease in contrast as previously described. In other words, it is concluded that the lowering of visual acuity in water with turbidity lower than 2 ppm is caused by the masking phenomenon dependent on suspended particles, while in the range of turbidity higher than 2 ppm it is influenced by the decrease in apparent contrast in addition to the masking phenomenon.

In the future, it will be necessary to conduct further experiments which change the distance from the eye to the target, as well as experi-

Table 3. Calculated target diameters at the limit of discrimination in water with different turbidity.

Turbidity (ppm)	Diameter (mm)
1	1.21
2	1.31
3	1.48

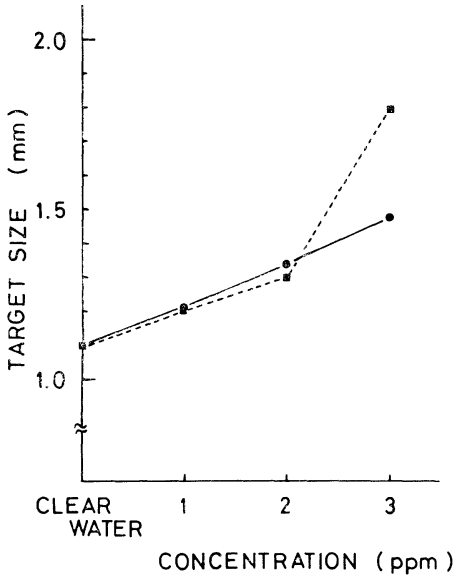

Fig. 7. Relationship between target diameter and turbidity at the limit of discrimiantion. Symbols ■ and ● stand for the experimental values and the theoretical values obtained by equation (3), respectively.

ments which change the contrast inherent to the target in order to elucidate the above-mentioned problems.

Acknowledgements

The authors wish to express their hearty thanks to Dr. Toshiro KUROKI, Professor of Nihon University, for his valuable guidance and advice in regard to this paper.

References

BRUNNER, G. (1934): Über die Sehschärfe der Elritze (*Phoxinus laevis*) bei verschiedenen Helligkeiten. Zeit. vergl. Physiol., **21**, 297-316.

HESTER, F. J. (1968): Visual contrast thresholds of the goldfish (*Carassius auratus*). Vision Res., **8**, 1315-1335.

KAHMANN, H. (1934): Über das Vorkommen einer *Fovea centralis* im Knochenfischauge. Zool. Anz., **106**, 49-56.

KAHMANN, H. (1936): Über das Foveale der Wirbeltiere. von Graefe's Arch. Ophthal., **135**, 265-276.

KAWAMURA, G. and T. TAMURA (1973): Morphogical studies on the retina of two teleosts *Scomber tapeinocephalus* and *Halichoeres poecilopterus*. Bull. Japan. Soc. Sci. Fish., **39**, 715-726.

NAKAMURA, E. L. (1968): Visual acuity of two tunas, *Katsuwonus pelamis* and *Euthynus affinis*. Copeia, **1968**, 40-48.

O'CONNELL, E. L. (1963): The structure of the eye of *Sardinop caerulea*, *Engrulis mordax*, and four other pelagic marine teleosts. J. Morphol., **113**, 287-329.

TAMURA, T. (1957): A study of visual perception in fish, especially on resolving power and accommodation. Bull. Japan. Soc. Sci. Fish., **22**, 536-557.

TAMURA, T. and W. J. WISBY (1963): The visual sense of pelagic fishes especially the visual axis and accommodation. Bull. Mar. Sci. Gulf Carib., **13**, 433-448.

YAMANOUCHI, T. (1956): The visual acuity of the coral fish *Microcanthus strigatus* (Cuvier and Valenscinnes). Publ. Seto Mar. Biol. Lab., **5**, 133-156.

水中の濁りと魚の視力との関係 (1)

松生　洽, 島津仁一, 中村善彦

要旨: 水中の濁りの魚の視力への影響は漁具や漁法の開発のための重要な要素である。本研究は実験魚としてコイを用い，水中の濁りと魚の視力との関係を学習法を用いて生態学的面から求めたものである。その結果，コイの視力は明るさが十分な場合，清澄な水中で 0.106 であり，1 ppm（青色光の光束消散係数 1.25 m^{-1}），2 ppm (2.50 m^{-1})，および 3 ppm (3.75 m^{-1}) の濁水中でそれぞれ 0.097, 0.090，および 0.065 である。次に水中の濁りによる視力の減少について見かけのコントラストと視角内に存在する懸濁粒子によるマスク現象の面から検討した。2 ppm 以下の濁った水の中では，視力の低下はマスク現象から理論的に導いた結果とよく一致する。2 ppm 以上ではマスク現象の他に見かけのコントラストの低下による影響が加算されていると結論される。

La mer 19: 165-170, 1981
Société franco-japonaise d'océanographie, Tokyo

XBT 記録のディジタル集録装置の開発と利用*

北川庄司**, 平　啓介**, 寺本俊彦**

A Digital Data Logger for the XBT*

Shoji KITAGAWA**, Keisuke TAIRA** and Toshihiko TERAMOTO**

Abstract: A technique used for XBT data logging is described. A voltage signal proportional to resistance of an XBT-thermistor is generated in a self-balancing bridge circuit. The signal is converted into 10-bit binary digit at a rate of 12 Hz and is stored in a micro-computer. Through the processing of the stored data, temperature at every 0.5 m depth is available with an accuracy better than 0.1°C. The data logger has worked well at more than 500 stations in 7 cruises since December 1977. As an example of observation and data processing, a temperature section along 30°N from 138°E to 148°E is presented. A spatial auto-correlation function of isotherm depths is also illustrated.

1. まえがき

サーミスタ（時定数 0.09～0.13 s）を組みこんだプローブを航走中の観測船から投下して，水温の鉛直分布を計測する XBT (Expendable Bathythermograph) が，我が国でも数多く用いられている。XBT のサーミスタは，並行に接着された導線（直径 0.09 mm の銅線）に接続されている。導線は，プローブに内蔵されたスプロールに巻かれており，プローブの落下に伴って自動的に繰り出される。導線の他端は船上のキャニスタに内蔵されたスプロールに巻かれており，船の航走に伴って自動的に繰り出され，導線に過度の張力が加わらないように工夫されている。XBT プローブを海中に投下することにより，導線の長さから決まる水深まで水温を連続的に計測することができる。現在，我々は 450 m および 750 m 用を主として用いている。

XBT プローブの深度は投下以後の経過時間に依存しており，この時間を測って深度を評価する。導線が繰り出されるとプローブの重さが減少し，落下速度も減少するので，時間と深度の関係は線型でない。水温変化に対するサーミスタの抵抗値の変化も非線型であり，アナログ演算回路で線型化することは容易でない。従来のアナログ記録計では，水温・水深とも非線型目盛の記録紙を使用している。黒潮の流軸を追跡しようとするような場合には，いくつかの基準層の水温値と指標水温の深度を迅速に知ることが要求される。このような特殊目的およびシステムのモニターのためにアナログ記録計利用が便利なこともある。しかし，XBT 観測の特徴は，荒天時でも小人数で迅速かつ確実に観測が実施でき，しかも必要に応じて水平および鉛直両方向に密な観測が実施できることである。このため，XBT による観測資料は一般にぼう大な量に達する。データ処理も迅速に行って始めて，XBT 観測は首尾一貫した効率的なものとなる。我々が XBT 記録の集録をディジタル化しようとする最大の理由はこの点にある。また，海洋資料の交換に際しては，"全記録にわたって3メートル毎に ±0.2°C の精度でか，あるいは直線的内挿値がどこででも，原記録から ±0.2°C 以内に入る様に決められた屈曲点毎に数字式で表現

* 1981年7月1日受理 Received July 1, 1981
** 東京大学海洋研究所，
〒164 東京都中野区南台1-15-1
Ocean Research Institute, University of Tokyo, Nakano, Tokyo, 164 Japan

されるべきである"（国際海洋資料交換便覧，海洋資料センター，昭和49年）ことが勧告されている。これらを達成するためにも，アナログ記録を用いることは実際的でない。

このような見地から，我々は XBT 記録のディジタル集録装置を開発し，すでに1977年から利用している。ここでディジタル集録装置とそれを使用して観測した北緯30度線上の水温構造について述べる。後者は TAIRA (1980) にその1部が記述されている。

2. ディジタル・データ集録装置

Fig. 1 に XBT プローブ（点線で囲ってある）とサーミスタの抵抗値（R_T）を検出するブリッジの等価回路を模式的に示した。サーミスタの一端は海水に接し，船体アースを通してブリッジ回路につながっている。抵抗 $r1$, $r2$ は2本の導線の抵抗であり，プローブ製造時は補正抵抗を挿入して，$r1=r2$ となるように調整されている。2本の導線は並行に接着されているので，銅線の抵抗が温度によって変化しても，両者は同じように変化し，$r1=r2$ の関係は変らないと考えてよい。Fig. 1 の T_r は 2SK 30A（接合型 FET）を示す。そのドレインとソース間の抵抗を R_{DS} で表わすことにする。Fig. 1 は，XBT 回路が4つの抵抗辺 $R1$, $R2$, $R_{DS}+r1$, R_T+r2 で構成されたホイートストン・ブリッジを構成することを示している。a-b 間の電位差が0になる条件は

$$R1(R_{DS}+r1)=R2(R_T+r2)$$

である。$R1=R2$ に選ぶと $R_T=R_{DS}$ のとき平衡になる。

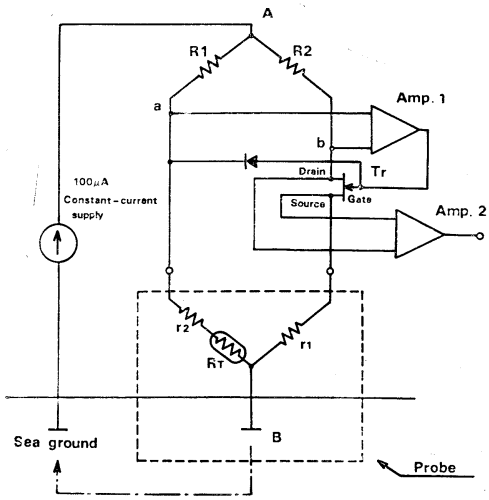

Fig. 1. Schematic diagram of self-balancing bridge, which generates voltage signal proportional to registance of the XBT-thermistor, R_T.

接合型 FET のドレインとソース間の抵抗は，リースとゲート間の電圧によって変えることができる (voltage-controlled registance)。Amp. 1 は a-b 間の電位差をなくするように，Tr のゲート電圧を変えるためのコンパレータである。a-b 間の電位差が0のとき，ブリッジに加えられる電流が一定であれば，Tr のドレインとソース間の電圧降下はサーミスタの抵抗 $R_T(=R_{DS})$ に比例する。ブリッジの両端 A-B に 100 μA の定電流を加えて，R_T に比例する電圧を Amp. 2 の出力として取り出すことにした。この回路は STEGEN *et al.* (1975) が用いたものである。市販の XBT アナログ記録計は，R_{DS} の代わりに自動平衡型記録計の摺動抵抗器を用いている。従って，この方式では記録計の外部に XBT の電圧信号をとり出すことはできない。

XBT プローブのサーミスタの抵抗値は 1°C 毎に測定されている。−2.0°C で 18094Ω, 25.0°C で 5000Ω, 35.0°C で 3263Ω などである。これらの抵抗値に比例した電圧値を A-D 変換器で数値化して取り出すこととする。10 ビットの A-D 変換器を用いて，例えば −2.0°C のとき 1023, 35.0°C のとき 184 となるようにする。すなわち，数値（電圧値）X とサーミスタ抵抗 R_T の関係を $X=1023\,R_T/18094$ とする。温度 T°C は X の対数 $x=lnX$ についての次の多項式で近似することができる。

$$T=a+bx+cx^2+dx^3+ex^4+fx^5 \quad (1)$$

ここで，$a=3391.180$, $b=-2683.387$, $c=876.365$, $d=-144.5101$, $e=11.91547$, $f=-0.3923869$ である。この近似式の誤差の標準偏差は，

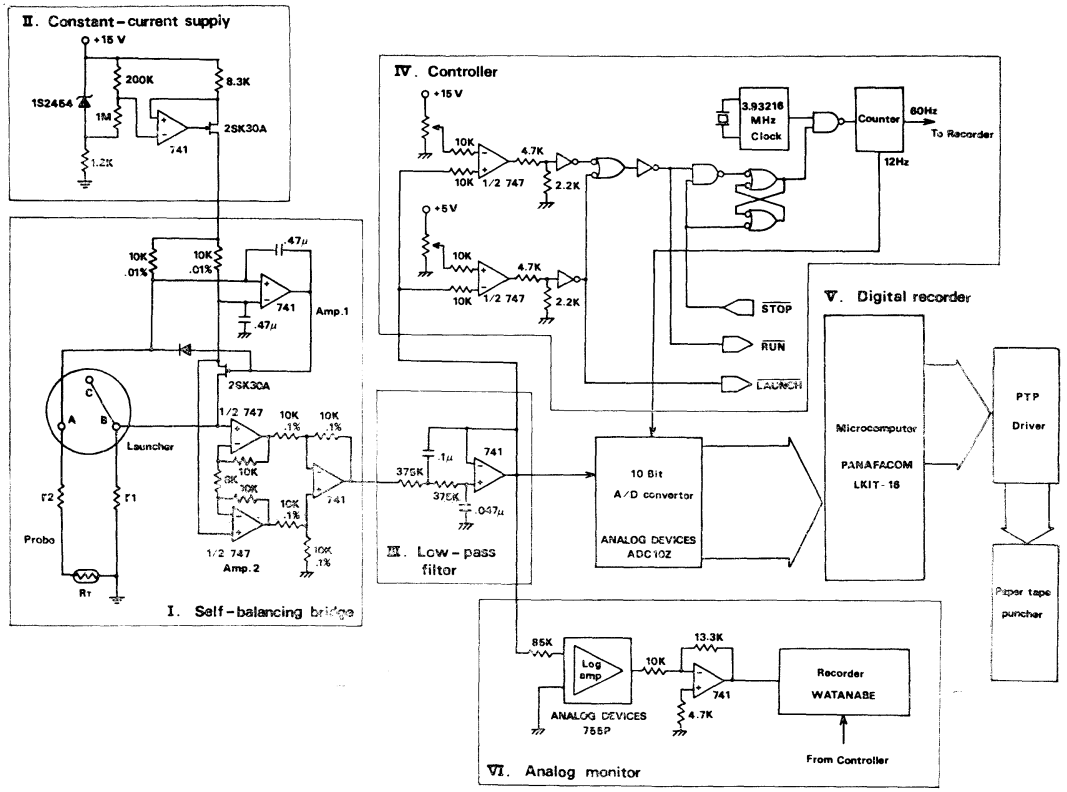

Fig. 2. Schematic diagram of the digital data logger for the XBT.

$-2.0°C \leqq T \leqq 35.0°C$ について，0.030°C である。近似誤差は高温部で大きく，35.0°C のとき 0.103°C になる。温度範囲を −2°C から 25°C までに限ると，標準偏差 0.0155°C，最大誤差 −0.029°C である。

XBT プローブの海面からの落下距離 H(m) は，経過時間を t とすると次の式で表現される (STEGEN *et al.*, 1975)。

$$H=6.472\,t-0.0216\,t^2 \qquad (2)$$

毎秒12回のサンプリングを行うと，約 50 cm 毎に測温することになり，内挿によって 1 m 毎の水温値が評価できる。

我々の目標とする分解能は，水温については 0.1°C，水深について 1 m である。上述のように，10ビットの A-D 変換器で毎秒12回のサンプリングでディジタル記録を集録すればよいことになる。Fig. 2 にディジタル集録装置の回路図を示す。6つの部分で構成されている。I がブリッジ，II が定電流回路である (Fig. 1)。XBT プローブには長い導線を使用しているため，外部ノイズが混入しやすい。Fig. 1 で示した Amp. 2 には差動増幅器を採用したので，外部ノイズを除去するうえでも効果的である。サンプリングのナイキスト周波数 (6 Hz) より高い周波数の成分は，III のローパス・フィルターで除去される。フィルターの遮断周波数は $f_c=6$ Hz で，$2f_c$ より高い周波数域で 12 dB/Oct の減衰特性をもっている。

ローパス・フィルターを通った出力電圧は次の3通りに変化する。(1) −15V (供給電源電圧)：ランチャーにプローブが装填されていないとき，およびプローブの導線が断線したとき。(2) +15 V (供給電源電圧)：ランチャーにプローブが装填されたとき。(3) +5V(−2°C)～0.8823 V (35.55 °C)：プローブが着水してブリッジ回路に定電流が供給され，サーミスタの抵抗値に比例した電圧

が出力されるとき。これらの電圧変化を判定して，IV の制御部は次のように動作する。LAUNCH の LED 表示：ランチャーにプローブが装填されたとき。RUN の LED 表示とパルス信号の出力：プローブが着水したとき。12 Hz のパルスをサンプリング信号として V の A-D 変換器へ，そして 60 Hz のパルスを紙送り駆動信号として VI のアナログ記録計へ，それぞれ出力する。STOP の LED 表示：プローブが落下して，導線が断線したとき。

ディジタル・データ集録部 (V) は，IV の制御部の 12 Hz のパルス信号に従って，フィルターの出力電圧を 10 ビットの 2 進数に変換する A-D 変換器と，その 2 進数をメモリに保持するマイクロ・コンピュータ (PANAFACOM LKIT-16) とで構成されている。制御部の STOP 表示で集録を終えて，メモリのデータをバイナリ形式で紙テープに穿孔出力する。ノイズによって STOP の LED が一時的に点灯することがあるので，データ集録の終了は観測者が判断する方式にした。出力された紙テープは，白鳳丸上のミニコンピュータ (NOVA 01) と海洋研究所の計算機 (FACOM M-160S) を用いて処理する。

VI の部分はアナログ・モニターである。サーミスタ抵抗値に比例した電圧を対数増幅器で線型化して，放電ペン書記録計（渡辺測器，Servocorder Type SR651）で記録する。専用のスケール板を用いて，水温値と深度を読みとることができるが，正常に計測が行われているかどうかのモニターのために主として使用している。

3. 観測例—北緯 30 度線上の水温構造

XBT による水温の鉛直分布測定の精度を，海洋現場での観測を通じて確かめることは一般に困難である。例えば，同一測点で CTD (Conductivity-Temperature-Depth) 観測を行なうと，XBT 観測の結果と非常に酷似した結果が得られるが，約 30分間の時刻のずれとその間の船のドリフトで，現場の水温分布が時・空間的に変化するので，両者の差が XBT 観測の誤差を示しているとはいえない。数多くの XBT プローブを使用する比較実験を行うことが考えられるが，これまで行っていない。ここでは，XBT を用いた東西断面の水温構造観測の例をあげ，我々の測定システムの効用の一端を示すこととする。

1977 年 12月17日から 19 日にかけて，北緯 30度線上，東経 138 度から 148 度まで 971 km の間の 32点で XBT 観測と 4 点で CTD (Plessey Environmental Systems, Model 9041)観測を行った(白鳳丸 KH-77-4 次航海)。これらの測温観測は約 27.7 km のほぼ等間隔で行われた。5 m 毎の深度に対する内挿値をもとに計算機サブルーチンを用いて描いた水温分布の断面図を Fig. 3 に示した。図の横軸に経度と測点番号（▲印は CTD 測点を示

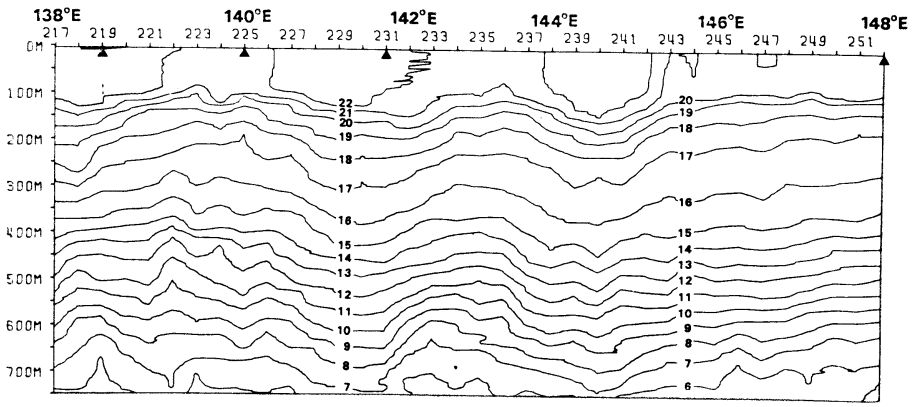

Fig. 3. Contour map of temperature section observed on December 17-19, 1977, along 30°N.

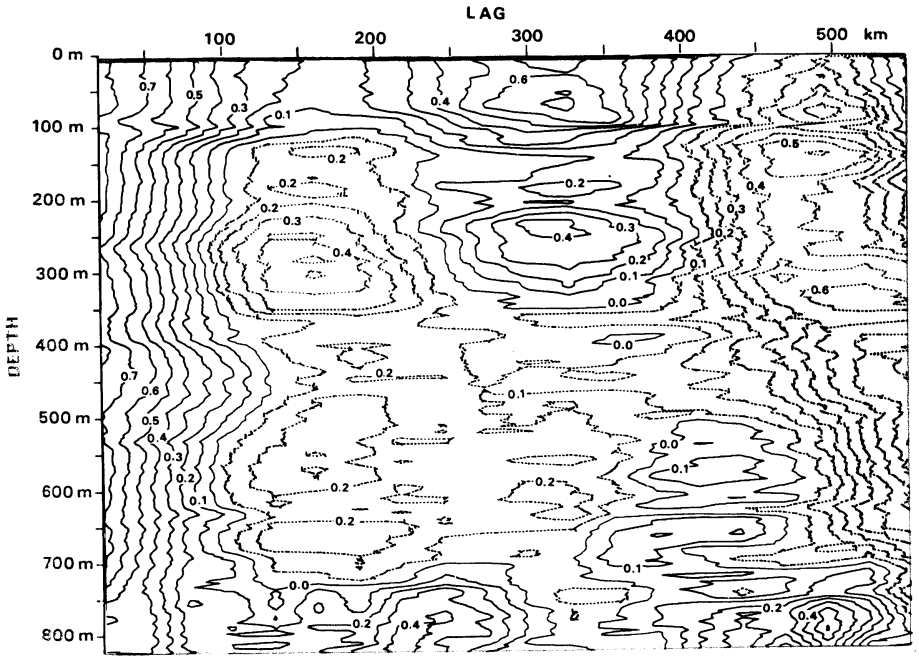

Fig. 4. Contour map of auto-correlation of the temperature section shown in Fig. 3.

す）を，縦軸に深度をとってある。測定に用いたXBT プローブは T-7（750 m）で，各点で820 m までの記録が得られたが，サブルーチンの制限により，Fig. 3 では 750 m までについて 1°C 毎の等値線を示した。このように等値線を自動的に描くことができることがディジタル・データ集録を行うことの利点の1つである。

Fig. 3 では，300～600 m 層で水温変化の勾配が大きい（サーモクライン）。約 350 m より上層と約 600 m より下層とでは，東西方向の卓越波長が明らかに異なっている。水温構造にみられる卓越波長を評価するために，5 m 毎の各層の 36 点について，最大ラグ数を20にとり，空間相関々数を算出した（Fig. 4）。図の横軸にずらし幅（km）をとり，縦軸に深度をとり，相関々数の 0.1 毎の等値線を示した。等値線は実線が正の値，点線が負の値を示している。深度 350 m より上層で，相関々数の極大値がラグ 320 km 付近に，そして極小値がラグ 160 km と 480 km 付近にある。卓越波長が約 320 km であることを示している。一方，深度 700 m より下層で，相関々数の極大値がラグ 240 km と 480 km 付近に，そして極小値がラグ 120 km と 360 km 付近にある。下層の卓越波長が約 240 km であることを示している。Fig. 4 でラグ 160 km 付近の極小値が上層から約700 m 層までのびていること，およびラグ 360 km 付近の極小値が下層から約 350 m 層までのびていることは，中間の 350 m～700 m 層では，上層と下層の卓越波長の変動が混在していることを示している。

水温・塩分の水平方向の分布のスペクトル解析によって，卓越波長が海域によって異なることが報告されている（BERNSTEIN and WHITE, 1974, 1977; RODEN, 1979）。我々の観測は，この海域では，深度によって卓越波長が異なることを示した。

4. あとがき

我々は本装置を用いて，すでに 500 回以上の XBT 観測を行ってきた。その結果をふまえ，今後次のことを改善して行きたい。データ集録の精度を 0.1°C としたが，測温の精度を高めるために，

個々の XBT プローブの温度特性を検定することが必要である。サーミスタ特性に経年変化（例えば，PAYNE *et al.*, 1976）があるからである。しかし，すでに述べたように，XBT プローブを海水に入れないとブリッジが構成できない。恒温槽で較正するとき，攪拌すると指示値が大きく変動し，電解分極の影響が大きいことがわかった。観測時の落下速度と等しい速度の流水中で較正することが必要である。次に，船上ではノイズが大きく，とりわけ船舶無線の発信中は XBT 観測が行えない。有効なノイズ対策が必要である。また現在船上に搭載されている計算機の多くが，IEEE 488 (GPIB), RS-232-C, SAIL などの汎用インターフェースを備えるようになってきたので，我々の集録装置の出力をこれらに合わせるようにして行きたい。

謝　辞

技術資料を提供された鈴木重教氏（株式会社鶴見精機）に感謝します。データ解析にあたって，深沢理郎，川口尚子，坂村由起子，木村典代（東京大学海洋研究所）の諸氏の助力を受けました。観測に協力された白鳳丸の乗組員に感謝します。

文　献

BERNSTEIN, R. L., and W. B. WHITE (1974): Time and length scales of baroclinic eddies in the central North Pacific Ocean. J. Phys. Oceanogr., **4**, 613-624.

BERNSTEIN, R. L., and W. B. WHITE (1977): Zonal variability in the distribution of eddy energy in the mid-latitude North Pacific Ocean. J. Phys. Oceanogr., **7**, 123-126.

PAYNE, R. E., A. L. BRADSHAW, J. P. DEAN and K. E. SCHLEICHER (1976): Accuracy of temperature measurements with the VACM. W.H.O.I. Ref. 76-94 (Unpublished Manuscript).

RODEN, G. I. (1979): The depth variability of meridional gradients of temperature, salinity and sound velocity in the western North Pacific. J. Phys. Oceanogr., **9**, 756-767.

STEGEN, G. R., D. P. DELIST and R. C. VON COLLN (1975): A portable, digital recording, expendable bathythermograph (XBT) system. Deep-Sea Res., **22**, 447-453.

TAIRA, K. (1980): Direct observations of current in the Kuroshio around the Izu Ridge. Doctoral Dissertation, University of Tokyo, 68 pp.

La mer 19: 171-178, 1981
Société franco-japonaise d'océanographie, Tokyo

Surface Temperature-Salinity Front in the Kuroshio South of Japan*

Isao TAKANO**, Shiro IMAWAKI*** and Hideaki KUNISHI***

Abstract: Distributions of surface temperature and salinity in the Kuroshio are examined from continuous records at nineteen crossings of the Kuroshio south of Japan in September 1975. A cold, low-salinity water spreads widely on the coastal side of the Kuroshio and a warm, high-salinity water spreads on the offshore side. There exist abrupt changes of temperature and salinity continuously along the Kuroshio axis, which are properly called a surface temperature-salinity front. Temperature and salinity differences of the front are 0.7°C and 0.6‰, respectively on averages. The width of the front is 3 km on an average and the thickness is about 20 m.

Density difference in the front is fairly small because density changes due to temperature difference and salinity difference tend to cancel each other, although the density is a little larger on the offshore side due to relatively large salinity difference. Sharpness of the front is not weakened in the meander region apart from the coast. A horizontal convergence required for the sharpness to be maintained is roughly estimated in a simple model to be about 10^{-5} sec^{-1}, which is comparable to observed surface convergences near the Kuroshio axis.

1. Introduction

In general, there are cold, low-salinity waters on the coastal side of the surface layer in the Kuroshio and warm, high-salinity waters on the offshore side. The Kuroshio region is the transition region between these two kinds of different waters. Water exchanges between these two waters are important, especially in problems of coastal water spreading. The way how these two waters are in contact with each other in the transition region, however, is not clearly understood.

FORD *et al.* (1952) observed water characteristics of the surface layer across the Gulf Stream and reported that a remarkable cold, low-salinity water is extended along the Gulf Stream on the coastal side of the axis. A similar cold, low-salinity water filament is described by WEBSTER (1961). VON ARX *et al.* (1955) discussed a fine structure of temperature and salinity and pointed out a frontal structure of the Gulf Stream near the axis. SAUNDERS (1971) pursued an anticyclonic eddy detached from the Gulf Stream for several months and reported the property changes of water contained within the eddy. FISHER (1972) examined an entrainment of the shelf water into the Gulf Stream and formation of a cold filament along the Gulf Stream by use of an airborne radiation thermometer. Recently, LEE *et al.* (1981) observed eddies formed at the front between the shelf water and the Gulf Stream water, and examined water exchange provided by the eddies. Near the Kuroshio, several works were done on temperature-salinity fronts in coastal regions (for example, YOSHIOKA, 1971; YANAGI, 1980) but few works were done on a water structure of the surface layer in the Kuroshio.

The surface layer is complicated due to effects of radiation, precipitation, evaporation, wind and so on. By a usual observation, whose station intervals are relatively wide, it is difficult to describe a detailed water structure of the surface layer. In the present work, frontal structure of the Kuroshio surface layer is investigated

* Received July 15, 1981
** Geophysical Institute, Faculty of Science, Kyoto University, Kyoto, 606 Japan
Present affiliation: Meteorological Satellite Center, Kiyose-shi, Tokyo, 180-04 Japan
*** Geophysical Institute, Faculty of Science, Kyoto University, Kyoto, 606 Japan

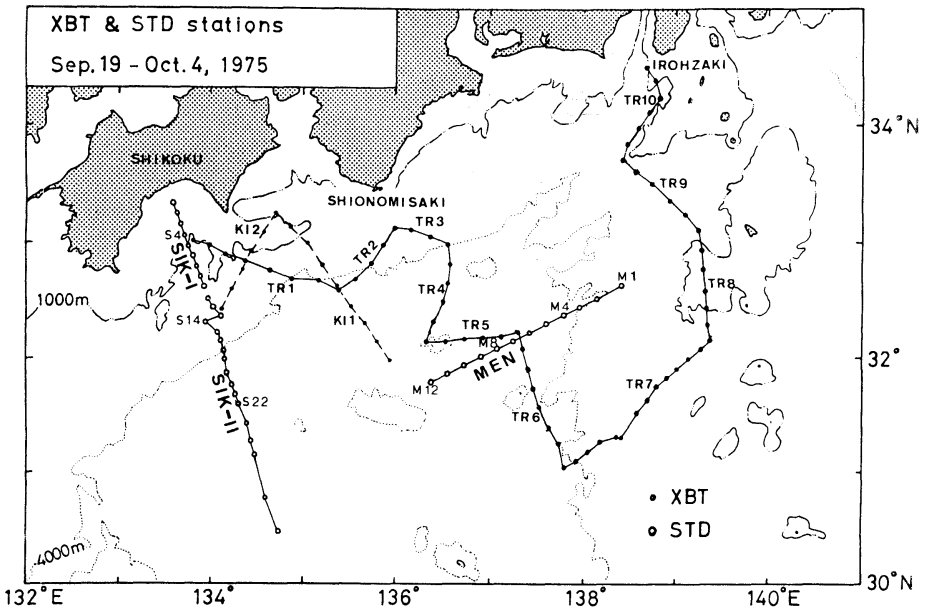

Fig. 1. A part of ship tracks and STD and XBT stations during the leg II of the Hakuho Maru Cruise KH-75-5 (September 19 to October 4, 1975).

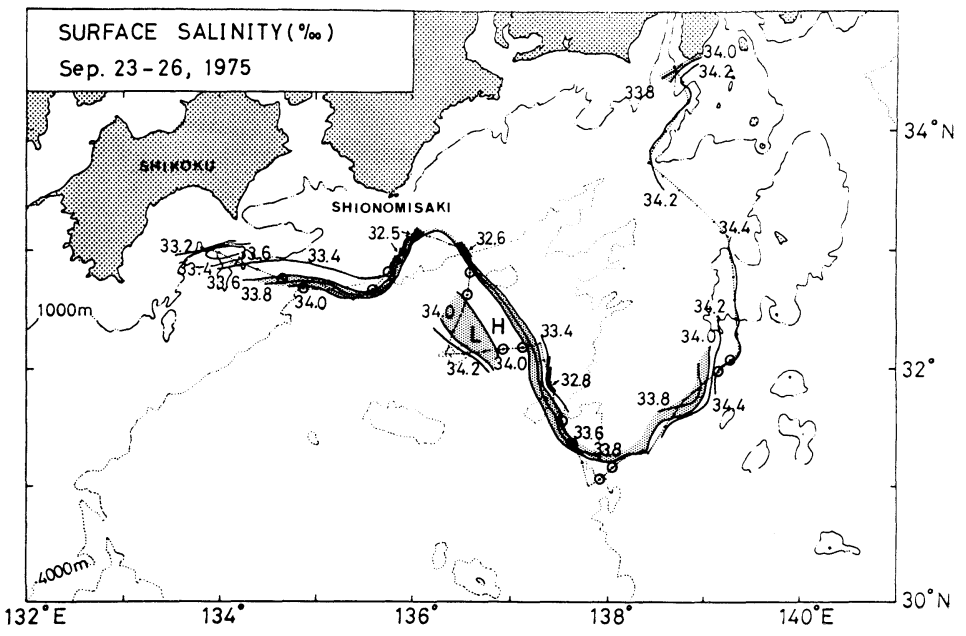

Fig. 2. Surface salinity distribution observed during the tracking of the Kuroshio (September 23 to 25, 1975) with a surface ST meter. Shaded area indicates the region where salinity is between 33.6‰ and 34.0‰. Open circles indicate locations of the Kuroshio axis determined from GEK velocities.

from continuous records of temperature and salinity.

2. Observation

The Kuroshio began to take a stationary meander path in August 1975. Just after the beginning of the meander, a detailed survey of the Kuroshio was carried out from September 19 to October 6 during the leg II in the Cruise KH-75-5 of the R.V. Hakuho Maru (KUNISHI *et al.*, 1978). Figure 1 shows a part of the ship track and locations of stations in the leg II. Continuous records of temperature and salinity of the surface water were obtained at many crossings of the Kuroshio by use of a surface ST (salinity-temperature) meter; it measured temperature and salinity of water pumped up at a depth of 5 m continuously underway. Resolutions of the records are 0.03°C for temperature and 0.006‰ for salinity. Surface currents were observed by GEK (geomagnetic electrokinetograph) at selected stations. Several temperature sections were also obtained with an XBT (expendable bathythermograph) system and two temperature and salinity sections (Sections SIK-I, II and MEN) were obtained with an STD (salinity-temperature-depth recorder).

3. Description of the front

A tracking of the Kuroshio was carried out by means of the XBT system and GEK (Lines TR1 to TR10). Figure 2 shows a distribution of surface salinity obtained during the tracking with the surface ST meter. Here locations of

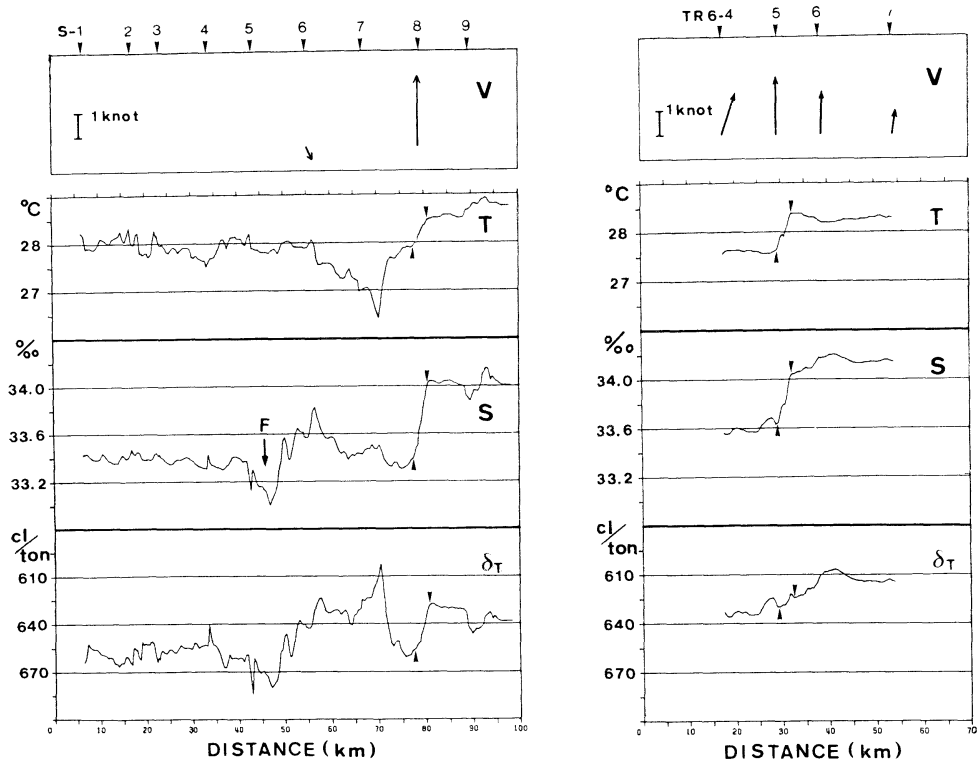

Fig. 3. Horizontal distributions of surface GEK velocity, temperature, salinity and the thermosteric anomaly across the Kuroshio (a) on Line SIK-I (September 22 to 23, 1975) and (b) on Line TR 6 (September 24, 1975). Records are projected on a line perpendicular to the Kuroshio axis. Coastal and offshore edges of the front are indicated by a pair of arrows in each panel. A symbol F indicates a fresh water.

the Kuroshio axis determined from GEK velocities are also shown by open circles. An isohaline of 34.0 ‰ roughly coincides with the Kuroshio axis. Salinity is relatively low on the coastal side and relatively high on the offshore side. Isohalines of 33.6 ‰ to 34.0 ‰ are closely spaced along the Kuroshio axis. On the other hand, surface salinity is fairly uniform both on the coastal side and on the offshore side of the Kuroshio axis; especially, it is seen in the distributions on Lines MEN and SIK-II, although they are not shown here. Namely, the low-salinity coastal water spreads widely on the coastal side and the high-salinity offshore water spreads widely on the offshore side. And there seems to be a narrow transition region between these two waters.

Horizontal distributions of surface temperature and salinity are carefully examined at nineteen crossings of the Kuroshio. Two of them are shown in Fig. 3, which illustrates horizontal distributions of temperature, salinity and the thermosteric anomaly (δ_T) (a) on Line SIK-I and (b) on Line TR6. Here scales of temperature and salinity are chosen so that their contributions to the density are equal to each other. Surface velocities observed by GEK are also shown in the uppermost panel. Since horizontal distributions of water properties perpendicular to the Kuroshio axis are intended to be examined, records are projected on a line normal to a direction of the strongest GEK velocity. Near the Kuroshio axis, temperature and salinity vary remarkably in a narrow interval. This abrupt change is called here a surface temperature-salinity front in the Kuroshio. On the coastal side of the front, surface temperature and salinity fluctuate a little in the slope region (in the present article, a region where the Kuroshio flows near the continental slope, such as off Shikoku, Shionomisaki, or Irohzaki, is called the slope region) and they are quite uniform in the meander region. On the offshore side of the front, temperature is almost uniform and salinity increases slightly as one leaves the front southward.

Figure 4 shows positions of the fronts and the Kuroshio axis observed during the tracking. Fronts exist continuously along the Kuroshio and they are close to the Kuroshio axis; more precisely, they are considered to be on the coastal side of the axis.

Horizontal variation of characteristics of the front along the Kuroshio is shown in Fig. 5.

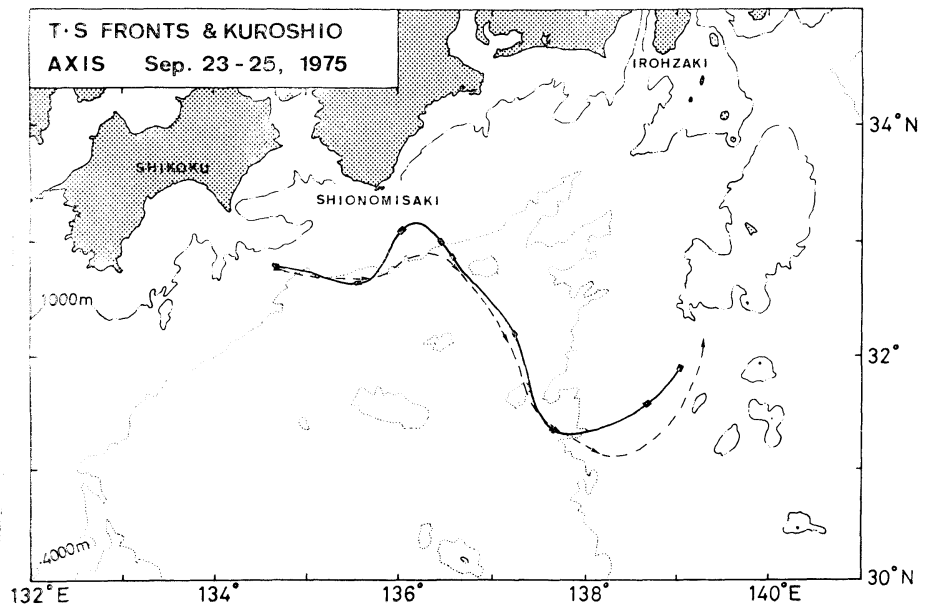

Fig. 4. Positions of the fronts (a solid line) and the Kuroshio axis (a broken line) observed during the tracking (September 23 to 25, 1975).

which illustrates variations of the width Δx, temperature difference ΔT, salinity difference ΔS, and the thermosteric anomaly difference $\Delta\delta_T$. The abscissa is the distance along the Kuroshio axis from off Shikoku to off Irohzaki. The slope region and the meander region are indicated at the bottom. Widths of the fronts vary 1 to 5 km with an average of 2.8 km, which is very narrow compared with the width of the Kuroshio of about 100 km. Although the width of the fronts varies a little from place to place, there are no remarkable differences in widths between the slope region and the meander region. Temperature differences are 0.5 to 1.2°C with an average of 0.74°C. Salinity differences are 0.4 to 1.1 ‰ with an average of 0.60 ‰. Salinity differences are larger in the slope region than in the meander region. Density changes due to temperature changes and those due to salinity changes in the front tend to cancel each other; i.e., an increase of temperature from the coastal side to the offshore side results in a decrease of the density, while an increase of salinity results in an increase of the density.

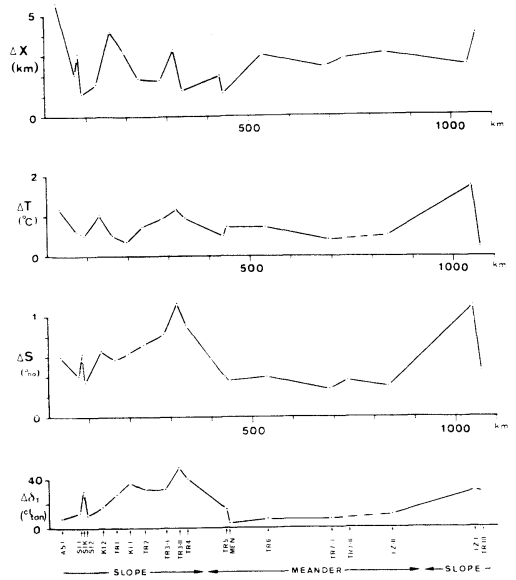

Fig. 5. Horizontal distributions of the width, temperature difference, salinity difference, and thermosteric anomaly difference in the front observed from September 19 to October 4, 1975. The abscissa is the distance along the Kuroshio axis.

Density increase due to salinity increase across the front is generally larger in the present cases than density decrease due to temperature increase. Therefore, the density is larger on the offshore side than on the coastal side. The thermosteric anomaly difference is about 30 cl/ton in the slope region. In the meander region, on the other hand, the density changes due to temperature changes and those due to salinity changes are almost equal to each other, resulting in a fairly small density difference.

Figure 6 shows a temperature section of Line TR6 obtained with the XBT system in the meander region. An isotherm of 28°C intersects the sea surface at the front. It is vertical to a depth of about 20 m. In the surface layer

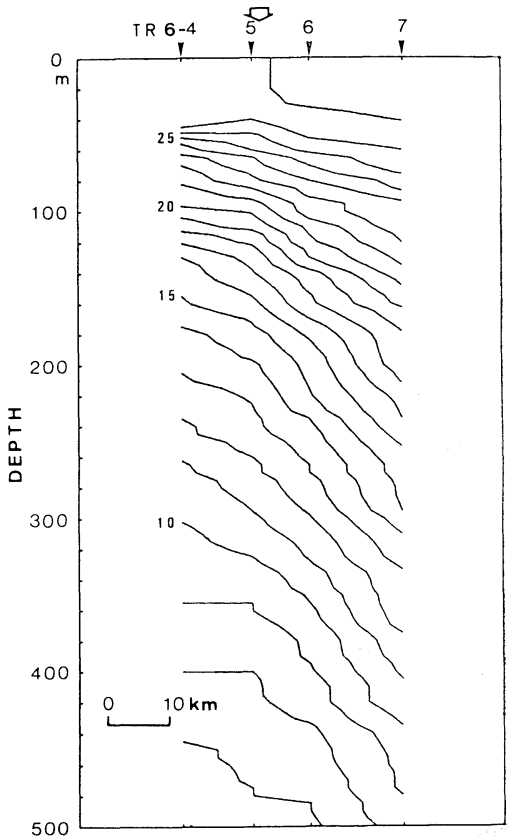

Fig. 6. Temperature (°C) section of Line TR6 obtained with an XBT system and projected on a section perpendicular to the Kuroshio axis. An open arrow shows the location of the surface front determined from the surface ST meter records.

of about 20 m thickness, temperature and salinity are vertically uniform. Hence the thickness of the front is considered to be the thickness of this surface mixed layer.

There are remarkably low-salinity waters on the coastal side of the front in the slope region as is seen, for example, in Fig. 3(a), indicated by a symbol F. Salinities are about 0.4‰ lower than those of the surrounding waters. Temperatures do not differ from those of the surrounding waters. The widths of these fresh waters are about 10 km. These fresh waters are considered to be originated from the coasts in Japan. In some cases, they come into contact with the front and are elongated along the front. Strong lateral shear of the Kuroshio on the coastal side presumably extends the fresh waters to long filaments.

Relatively low-salinity waters are also found on the offshore side of the front at some crossings. Salinities are about 0.2‰ lower than those of the surrounding waters. Widths are about 10 km. These waters, however, have no sharp boundaries as the fresh waters on the coastal side. KURODA (1969) also observed relatively low-salinity waters with large diatom populations on the offshore side of the Kuroshio and suggested that the waters may be originated from the coasts. Existence of these relatively low-salinity waters indicates that water exchanges take place across the front.

4. Discussion

The surface temperature-salinity front exists along the Kuroshio and is located very close to the Kuroshio axis. The front is very sharp and is not weakened in the meander region apart from the coast. These features suggest that some mechanism maintaining the sharpness should exist. For the sharpness of the front to be maintained, the cold, low-salinity water should be always supplied from the coastal side of the front and the warm, high-salinity water should be from the offshore side of the front; i.e., horizontal convergence should occur in the front. Strength of the horizontal convergence is roughly estimated in a simple model (Fig. 7). Salinity of the surface layer is denoted by S on the coastal side and $S+\Delta S$ on the offshore

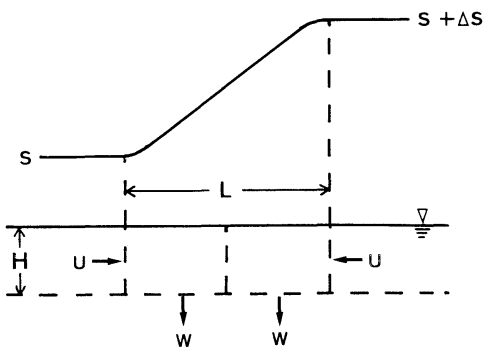

Fig. 7. A convergence model of the surface temperature-salinity front in the Kuroshio. Upper is a horizontal distribution of salinity and lower is a vertical section of the front.

side. Salinity varies linearly in the front. Width and depth of the front are L and H, respectively. At the coastal and offshore edges of the front are assumed existences of horizontal flows with a normal component u toward the center of the front. Horizontal velocity is assumed to be zero at the center. At the bottom of the front, a downward flow w is assumed. Variations of velocities and water properties along the front are not taken into account. A steady state is considered, and precipitation and evaporation at the sea surface are neglected. Conservations of the mass and salinity in the coastal side box are

$$uH=\frac{1}{2}wL$$

$$uSH+K\frac{\Delta S}{L}H=w\left(S+\frac{\Delta S}{4}\right)\frac{L}{2},$$

where K is the horizontal eddy diffusivity coefficient. Elimination of u gives $w=8KH/L^2$. The same result is obtained in the offshore side box. A horizontal convergence is estimated as

$$-div\ \boldsymbol{V}=\frac{w}{H}=\frac{8K}{L^2}.$$

It implies that the strength of convergence depends on the horizontal scale as well as the eddy diffusivity. When K is $10^5 cm^2/sec$, L 3 km, and H 20 m, the convergence is estimated to be $0.9\times10^{-5}\,sec^{-1}$.

KAWAI *et al.* (1969) observed horizontal con-

vergences in the surface layer of the Kuroshio off Shikoku by use of floating buoys and proposed an existence of convergence zone of 10^{-4} to 10^{-5} sec^{-1} on the coastal side of the Kuroshio axis. The surface temperature-salinity front described in the present article seems to coincide with this convergence zone though further detailed surveys are needed for a firm conclusion.

The surface front in the Gulf Stream observed by VON ARX *et al.* (1955) has a temperature difference of about 2°C and a salinity difference of about 1‰. They are larger than those of the present surface front in the Kuroshio. The front in the Gulf Stream is also located on the coastal side of the Gulf Stream axis.

Because the Kuroshio axis changes its position with time, rapid observations are necessary for the whole system of the front to be investigated correctly. Sparsely-spaced observation stations tend to miss small features, such as small-scale meanders of the front or fresh water filaments on the coastal side of the Kuroshio. Temperature observations by means of airborne radiation thermometers (for example, FISHER, 1972) and by satellite infrared images (for example, LEE *et al.*, 1981) are very effective for these problems.

Acknowledgements

The authors would like to thank Chief Scientist T. TERAMOTO and other scientists who participated in the Cruise KH-75-5 of the R.V. Hakuho Maru of the University of Tokyo for their kind cooperation. Thanks are due to Captain I. TADAMA and other officers and crew of the Hakuho Maru for their skillful assistance. The surface ST meter was made by Mr. K. NISHI in Kyoto University. Measurements of surface temperature and salinity were carried out in cooperation with Mr. M. OKAZAKI in the Institute of Physical and Chemical Research. Acknowledgement is due to Professor H. KAWAI of Kyoto University for valuable discussion. The data were processed on a FACOM M-200 at the Data Processing Center, Kyoto University.

References

FISHER, A., Jr. (1972): Entrainment of Shelf Water by the Gulf Stream northeast of Cape Hatteras. J. Geophys. Res., **77**, 3248-3255.

FORD, W. L., J. R. LONGARD and R. E. BANKS (1952): On the nature, occurrence and origin of cold low-salinity water along the edge of the Gulf Stream. J. Marine Res., **11**, 281-293.

KAWAI, H., H. SAKAMOTO and M. MOMOTA (1969): A study on convergence and divergence in surface layer of the Kuroshio—I: Direct measurement and interpretation of convergence and divergence at the surface. Bull. Nansei Regional Fisheries Research Laboratory, **1**, 1-14 (in Japanese with an English abstract).

KUNISHI, H., S. IMAWAKI, M. ODAMAKI, A. HARASHIMA, S. ENDO, M. OKAZAKI and S. NAKAI (1978): Tracking and cross sections of the Kuroshio with a meander. *In*: T. TERAMOTO (ed.), Preliminary Report of the Hakuho Maru Cruise KH-75-5. Ocean Research Institute, Univ. Tokyo, 56 pp.

KURODA, K. (1969): Short-term variations of the surface diatoms in the Kuroshio. Oceanogr. Magazine, **21**, 97-111.

LEE, T. N., L. P. ATKINSON and R. LEGECKIS (1981): Observations of a Gulf Stream frontal eddy on the Georgia continental shelf, April 1977. Deep-Sea Res., **28**, 347-378.

SAUNDERS, P. M. (1971): Anticyclonic eddies formed from shoreward meanders of the Gulf Stream. Deep-Sea Res., **18**, 1207-1219.

VON ARX, W. S., D. F. BUMPUS and W. S. RICHARDSON (1955): On the fine structure of the Gulf Stream front. Deep-Sea Res., **3**, 46-65.

YANAGI, T. (1980): A coastal front in the Sea of Iyo. J. Oceanogr. Soc. Japan, **35**, 253-260.

YOSHIOKA, Y. (1971): Oceanic front at Kii-Suido in winter (1). Umi to Sora, **46**, 31-44 (in Japanese with an English abstract).

WEBSTER, F. (1961): A description of Gulf Stream meanders off Onslow Bay. Deep-Sea Res., **8**, 130-143.

本州南方黒潮表層の水温・塩分フロント

高野　功, 今脇資郎, 國司秀明

要旨: 1975年9月に本州南方の黒潮を横断する19本の測線上で得られた連続記録から，表層の水温，塩分の分布を調べた。黒潮の沿岸側には低温低塩分水が広く分布し，沖合側には高温高塩分水が広く分布している。黒潮流軸に沿って連続的に，表層の水温・塩分フロントと呼ばれるべき，水温と塩分の急変する部分が存在している。フロントにおける水温差と塩分差は平均してそれぞれ 0.7°C と 0.6‰ である。フロントの幅は平均して 3 km であり，厚さは 20 m 程度である。

フロントにおいては，水温差による密度変化と塩分差による密度変化が互いに打消し合う傾向にあり，フロントでの密度差はかなり小さい。ただし，このフロントでは塩分差の方がやや大きいため，密度は沖合側の方がやや大きくなっている。フロントの鋭さは，沿岸域から離れた蛇行域においても弱まっていない。この鋭さが維持されるために必要な水平収束の大きさを，簡単なモデルで見積ると約 $10^{-5}\,\mathrm{sec}^{-1}$ になる。これは黒潮流軸付近で観測された表層の水平収束の大きさと同程度である。

La mer 19: 179-184, 1981
Société franco-japonaise d'océanographie, Tokyo

2台のカメラによる海産魚類の群れ構造の三次元的解析*

長谷川 英一**, 坪井 均***

A Study on the Three-Dimensional Structure of Marine Fish Schools by the Stereo Method with Two Cameras*

Eiichi HASEGAWA** and Hitoshi TSUBOI***

Abstract: A stereo method with two cameras was used to determine the three-dimensional position of schools of marine fish in the tank. Photographs of fish schools in the tank were taken with two cameras set above it, and the depth of an individual position from the water surface was determined by the horizontal parallax estimated from two films. The average absolute errors were 1.4 cm in vertical direction and 0.4 cm in horizontal direction.

The structure of schools of sardine *Sardinops melanosticta*, parrot bass *Oplegnathus fasciatus*, striped pigfish *Parapristipoma trilineatum* and opaleye *Girella punctata* observed using this method was discussed with respect to the density of the school, the distance between the fish and the angular deviation of the school.

1. 緒 言

魚類の群れ構造を三次元的に測定した研究として CULLEN *et al.* (1965), SYMONS (1971), PITCHER (1973), 井上ら (1979) 等の報告がみられるが, 群れ構造の特徴を知ることは, その魚種に適合した漁具を設計し, さらにその漁具を運用する上で有効な情報となる。

本研究では, 水槽の上方に2台のカメラを水平に設置し, 水の屈折を考慮した独自の解析方法を考え, さらにその方法を使用してマイワシ *Sardinops melanosticta*, イシダイ *Oplegnathus fasciatus*, イサキ *Parapristipoma trilineatum* およびメジナ *Girella punctata* 等の群れ構造を測定したので報告する。

* 1981年8月20日受理 Received August 20, 1981
** 日本大学農獣医学部,
〒154 東京都世田谷区下馬3-34-1
College of Agriculture and Veterinary Medicine, Nihon University, Shimouma 3-34-1, Setagaya-ku, Tokyo, 154 Japan
*** リョービ株式会社 〒726 広島県府中市目崎町762
Ryobi Co., Ltd., Mesaki-cho 762, Fuchu-shi, Hiroshima, 726 Japan

2. 解析方法

2台のカメラを水槽上方に水平に設置し, 写真撮影を行ない, 2枚のフィルム面上での視差から水槽内の魚の三次元的位置を, 吻端と尾端の座標として求める。

屈折率 n の液体の液面下 h の深さにある物体の位置を Fig. 1 を参考にして解く。

側面図の右側のカメラについて

$$\overline{AP}=\overline{RO_1}+\overline{AQ}, \qquad (1)$$

$\triangle O_1'RO_1 \backsim \triangle O_1'R'P'$ より

$$\overline{RO_1}=Ha_1/f, \qquad (2)$$

また

$$\overline{AQ}=\overline{QR}\tan r.$$

ここで $\sin i/\sin r=n$, $\sin i=a_1/(a_1^2+f^2)^{1/2}$ より

$$\overline{AQ}=a_1h/\{(a_1^2+f^2)n^2-a_1^2\}^{1/2}. \qquad (3)$$

(1), (2), (3) より

$$x_1=Ha_1/f+a_1h/\{(a_1^2+f^2)n^2-a_1^2\}^{1/2}. \qquad (4)$$

左側のカメラについても同様にして

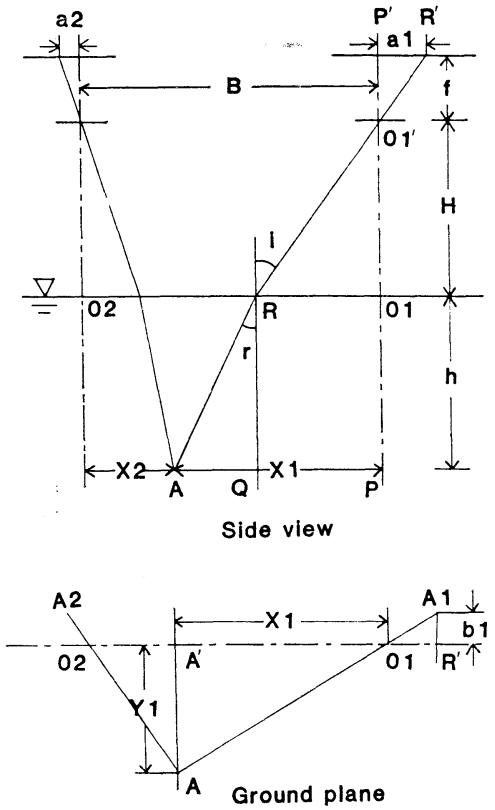

Fig. 1. Diagam of correcting X, Y and Z by photographs as taken from above.
A, object; *i*, angle of incidence; *r*, angle of refraction; *f*, focal distance; *B*, base line distance; *a*1 and *a*2, length of *X* coordinate on a film; *X*1 and *X*2, measured length of *X* coordinate; *b*1, length of *Y* coordinate on a film; *Y*1, measured length of *Y* coorditate.

$$x_2=Ha_2/f+a_2h/\{(a_2^2+f^2)n^2-a_2^2\}^{1/2}. \quad (5)$$

また

$$x_1+x_2=B. \quad (6)$$

(4), (5), (6) より

$$h=\{B-H(a_1+a_2)/f\}/[a_1/\{(a_1^2+f^2)n^2-a_1^2\}^{1/2}+a_2/\{(a_2^2+f^2)n^2-a_2^2\}^{1/2}].$$

また，平面図において $\triangle O_1AA'\backsim\triangle O_1A_1R'$ より

$$y_1=b_1x_1/a_1.$$

以上により O_1 を原点とする物体 A の座標 (x_1, y_1, h) が求まる。

上記の方法により測定誤差を調べた。球形のウキ3個を 10 cm 間隔でてぐすに連結したものを4本用意し，おもりをつけ水中に設置した。2台のカメラの光軸間距離 16.6 cm，カメラから水面までの距離 158 cm という状態でこれを撮影し，フィルムを約6倍に引き伸し，キャリパーを使用して視差を 0.05 mm 単位まで測定した。その結果，実測値と測定置の絶対誤差の平均値は深さ方向で 1.4 cm，水平方向で 0.4 cm となった。

次に各測定項目の定義であるが，個体間距離は魚の吻端間の距離をもって示し，2尾の吻端の座標を (x_i, y_i, z_i), (x_j, y_j, z_j) とした時に $\{(x_i-x_j)^2+(y_i-y_j)^2+(z_i-z_j)^2\}^{1/2}$ となる。ただし，x, y, z はそれぞれ群れの進行方向，横方向，深さ方向を表わす。群れの中の各個体同士の個体距離のうち最も近傍に位置する個体同士の値が最近傍個体間距離である。n 尾で形成された群の重心 (x_G, y_G, z_G)は，群れを形成する各個体の吻端の座標を (x_k, y_k, z_k) としたときに，$x_G=\sum_{k=1}^{n} x_k/n$, $y_G=\sum_{k=1}^{n} y_k/n$, $z_G=\sum_{k=1}^{n} z_k/n$ となる。また，群れを形成する各個体の位置の標準偏差 SX, SY, SZ を $SX=\{\sum_{k=1}^{n}(x_k-x_G)\}^{1/2}/n$, $SY=\{\sum_{k=1}^{n}(y_k-y_G)\}^{1/2}/n$, $SZ=\{\sum_{k=1}^{n}(z_k-z_G)\}^{1/2}/n$ の式で求め，魚の体長を a, 体幅を b, 体高を c として $(n\cdot a\cdot b\cdot c)/(SX\cdot SY\cdot SZ)$ なる式を密度指数とした。偏向角度は群れ全体の進行方向に対する各個体の角度のことで，x 軸に対する各個体の角度を θ_k とした時に $|\theta_G-\theta_k|$ で表わした。ただし，θ_G は群れの進行方向で，$\sum_{k=1}^{n}\theta_k/n$ である。

3. 実験方法

実験に使用した水槽は東京水産大学館山実験場の 450×150×70 cm の屋内コンクリート水槽で，撮影には Canon AE-1 2台を使用した。レンズの焦点距離は何れも 50 mm であるが，F 値は 1.8 と 1.4 である。この2台のカメラを光軸間距離 16 cm で水槽底面から 215 cm 上方に水平に設置し，2本のワイヤーレリーズでシャッターを同時に切った。

Table 1. Relation among the number of fish in a school, the density of the school and the extension of fish school in three dimensions.

	Sardine (*S. melanosticta*)			Parrot bass (*O. fasciatus*)		
Item＼Number of fish	5	10	14	5	10	15
X cm	19.6	36.8	26.5	18.9	27.8	31.2
Y cm	8.4	26.2	23.2	6.7	18.6	25.5
Z cm	10.4	17.5	9.1	12.1	12.4	20.8
Index of density	0.35	0.09	0.62			

水槽を水面から 2 m の距離にある 2 本の 30 W 白色蛍光灯で照明し，撮影時にはさらに撮影用ライト 2 個を用いた。その時の水中照度は 370 lx となった。また，実験時の水温は 19～24°C であった。

実験に供した魚種は館山湾内の生簀で蓄養されていた平均体長 5.7 cm のマイワシと体長 15～18 cm のイシダイで，体長 15 cm 未満のイシダイおよびイサキは定置網で捕獲されたものを使用した。また，メジナは釣獲後約 1 ケ月経過したものを使用した。

4. 結　果

(1) 群れ形成個体数と群れ構造

群れ構造が群れ形成個体数によってどのように変化するのかを次の実験により調べた。マイワシおよびイシダイを使用し，各々の群れ形成個体数を 5, 10, 14 尾（イシダイは 15 尾）と変化させ，X 軸方向，Y 軸方向，Z 軸方向の群れの広がりと密度について比較した。測定結果を Table 1 に示す。マイワシ群の場合は，群れ形成個体数が増加するに従い横方向の相対的比率が増加し，深さ方向の比率は減少している。一方，イシダイ群の場合では，群れ形成個体数が増加するに従い各方向に一様な広がりをみせ，群れの平面的形状は縦長から円型に変化する傾向となった。次に，マイワシ群の最近傍個体間距離の頻度分布を Fig. 2 に，偏向角度分布を Fig. 3 に示す。最近傍個体間距離の平均値は 5, 10, 14 尾群でそれぞれ 5.6, 8.3, 5.2 cm とバラツキがあるものの，モードは何れの場合も 5～6 cm で体長とほぼ等しい値となった。偏向角度の平均値は 5, 10, 14 尾群でそれぞれ

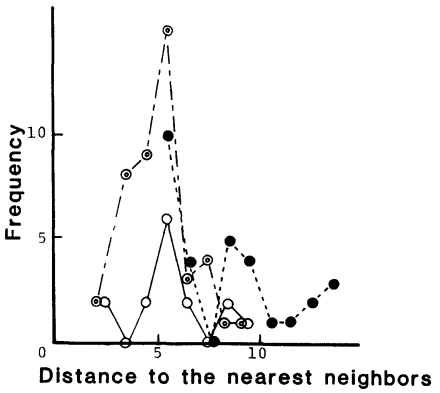

Fig. 2. Frequency distribution of the distance (cm) from fish to their nearest neighbors in sardine school. ○—○, 5 fish; ●···●, 10 fish; ◎-·-◎, 14 fish.

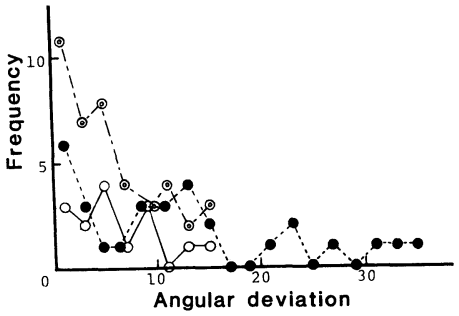

Fig. 3. Frequency distribution of the angular deviation between fish and their school in sardine. ○—○, 5 fish; ●···●, 10 fish; ◎-·-◎, 14 fish.

6, 13, 6 度となり，密度指数の小さい 10 尾群で群れの平行性が劣るという結果となった。群れを形成する各個体の群れの重心からの距離と偏向角度との関係を Fig. 4 に示す。5, 10 尾群では明らかではないが，14 尾群では重心から 5 cm 以内に位

置する個体の向きは群れの進行方向にほぼ一致していた。

（2） 魚種による群れ構造の比較

イサキの5尾群，メジナの4尾群，イシダイの5尾群を使用し，魚種による群れ構造の相違を調べた。これら3魚種の群れの広がりおよび密度指数の測定結果を Table 2 に示す。イシダイ群では密度指数が6.7と密な群れになったのに比べ，イサキ群，メジナ群ではそれぞれ 0.6，0.2 と疎な群れとなった。群れの形は何れの魚種とも進行方向に長い形であったが，イサキ，メジナ，イシダイと体長に対する体高の比率（イサキ：0.30，メジナ：0.40，イシダイ：0.47）が大きくなるにつれて進行方向に対する深さ方向の割合が大きくなり，横方向の割合が小さくなった。次に，これら3魚群の最近傍個体間距離と偏向角度の頻度分布の測定結果を Fig. 5 と Fig. 6 に示す。最近傍個体間距離の平均値はイサキ群，メジナ群，イシダイ群でそれぞれ 12.1 cm (1.4 B.L.)，13.0 cm (1.7 B.L.)，5.3 cm (0.6 B.L.) となり，イシダイ群が最も近

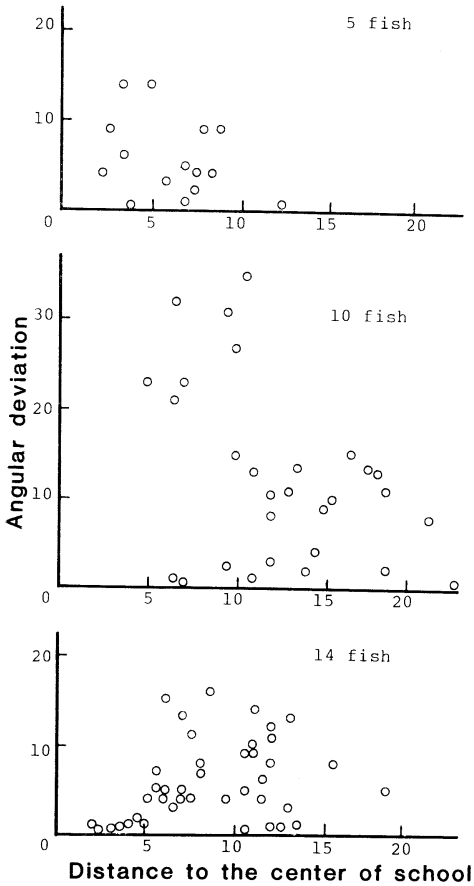

Fig. 4. Relation between the distance (cm) from fish to the center of their school and the angular deviation in sardine.

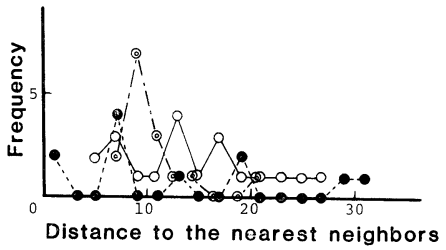

Fig. 5. Frequency distribution of the distance (cm) from fish to their nearest neighbors. ○—○, striped pigfish; ●···●, opaleye; ◎-·-◎, parrot bass.

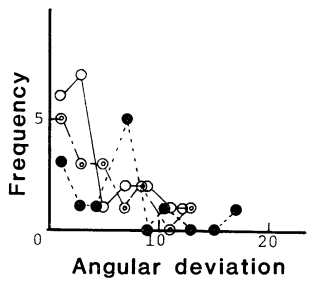

Fig. 6. Frequency distribution of the angular deviation between fish and their school. ○—○, striped pigfish; ●···●, opaleye; ◎-·-◎, parrot bass.

Table 2. Relation among the fish species, the density of the school and the extension of fish school in three dimensions.

Species	*X*	*Y*	*Z*	Index of density
Striped pigfish (*P. trilineatum*)	32.2	24.8	9.0	0.6
Opaleye (*G. punctata*)	33.2	19.6	14.4	0.2
Parrot bass (*O. fasciatus*)	18.9	6.7	12.1	6.7

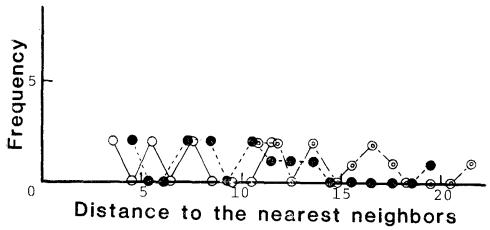

Fig. 7. Frequency distribution of the distance (cm) from fish to their nearest neighbors in parrot bass school. Mean B.L.: ○—○, 9.0 cm; ●…●, 12.0 cm; ◎-•-◎, 17.0 cm.

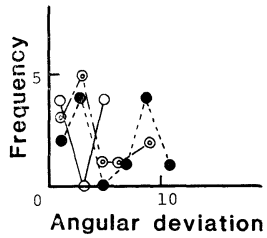

Fig. 8. Frequency distribution of the angular deviation between fish and their school in parrot bass. Mean B.L.: ○—○, 9.0 cm; ●…●, 12.0 cm; ◎-•-◎, 17.0 cm.

接した遊泳をしていることがわかるが，これは密度指数の結果とよく一致している。偏向角度の平均値は，それぞれ 4，6，4度となり魚種間の相違は余り見られなかった。

（3） 群れ形成個体の体長と群れ構造

群れ形成個体の体長の違いが群れ構造におよぼす影響を，平均体長 9，12，17 cm の3種のイシダイ群を使用して調べた。最近傍個体間距離と偏向角度の頻度分布を Fig. 7 と Fig. 8 に示す。最近傍個体間距離の平均値は群れの平均体長の小さい順に 7.2，9.9，14.7 cm となり，これを体長の何倍かで示すと何れも約 0.8 B.L. と一定している。また，偏向角度の平均値は群れの平均体長の小さい順に 3，6，4度となり，魚体長の影響は認められなかった。

5. 考　察

群れ形成個体数の増加に伴い群れの平面的形状は縦長から円型に変化する傾向がみられたが，これは個体数の増加に伴う群れの中での各個体の位置選択の変化の結果と思われる。また，14尾群の X，Y，Z 軸各方向への群れの広がりの相対比は 2.9 対 2.5 対 1.0 となり，RADAKOV (1973) の浮魚の群れの形は長さ，幅ともに 200～300 m で高さが 100～150 m であるという見解とほぼ同率であり，井上ら (1979) の報告にもあるように，群れを形成する各個体の相互視認に基づく位置選択が上下方向より，左右方向に大きく広がる傾向をもたらしたものと考える。群れを形成する各個体の群れの重心からの距離と偏向角度との関係では，先頭魚が特に他の魚より群れの進行方向に近いということはなかったが，このことは群れの進行方向が常に変化しうることを示唆する。

魚種による群れ構造の比較では，井上ら (1979) が淡水魚のバラタナゴ *Rhodeus ocellatus* とアブラハヤ *Moroco steindachneri* を供試魚として，群れ形成個体の魚体形と群れの外観構造の類似性を指摘しているが，海産魚を使用した本研究においても同様の結果となった。

OLST and HUNTER (1970) によると，群れはその形成個体の体長がある値以上になると個体間距離が安定し，その時の体長は魚種によっても異なるが大体 5～9 cm という値であると述べている。本研究で使用したイシダイは最小でも 8.5 cm であり，充分，個体間距離の安定した群れになる体長であると考えられるので，最近傍個体間距離の平均値が平均体長 9，12，17 cm 何れの場合でも約 0.8 B.L. と一定していたことは納得される。

6. 要　約

水槽の上方に2台のカメラを設置し，海産魚の群れ構造を stereo method により調べ，次の結果を得た。

（1） 群れ形成個体数の増加に従い，群れの広がりは，マイワシ群では横方向の相対的比率が増加し，深さ方向の比率は減少した。一方，イシダイ群では各方向に一様な広がりをみせ，群れの平面的形状は円型に近づく傾向をみせた。

（2） 群れ形成個体の魚体形と群れの外観構造の類似性が海産魚においても認められた。

（3） 群れを形成している各個体間の最近傍個体間距離の平均値は，群れ形成個体の平均体長に

関わらず約 0.8 B.L. で一定していた。

本稿を終るに当り，御校閲をいただいた東京水産大学井上実教授に深謝します。

文　　献

CULLEN, J. M., E. SHAW, and H. A. BALDWIN (1965): Methods for measuring the three-dimensional structure of fish schools. Anim. Behav., **13**, 534-547.

井上　実・長谷川英一・有元貴文 (1979): バラタナゴおよびアブラハヤの群れ構造の光学的測定とその解析. うみ, **17**: 92-103.

OLST, J. C. V. and J. R. HUNTER (1970): Some aspects of the organization of fish schools. J. Fish. Res. Bd. Canada, **27**, 1225-1238.

PITCHER, T. J. (1973): The three-dimensional structure of fish schools in the minnow, *Phoxinus Phoxinus* (*L.*). Anim. Behav., **21**, 673-686.

RADAKOV, D. V. (1973): Schooling in the ecology of fish. Israel Program for Scientific Translations. 173 pp.

SYMONS, P. E. K. (1971): Estimating distances between fish schooling in an aquarium. J. Fish. Res. Bd. Canada, **28**, 1805-1806.

La mer 19: 185-203, 1981
Société franco-japonaise d'océanographie, Tokyo

A Note on the Haline, Thermohaline and Thermohaline-Wind-Driven Ocean Circulation*

Kenzo TAKANO**

Résumé: Des expériences numériques ont été effectuées pour comprendre dans quelle mesure la circulation générale dans un océan à profondeur constante dépend du flux de salinité de surface, du flux de chaleur de surface et de la force d'entraînement du vent. Le flux de salinité de surface affaiblit la circulation et augmente les températures à des couches intermédiaires. La force d'entraînement du vent intensifie la circulation, augmente les températures et salinités de surface mais diminue la température moyenne de tout le bassin. En renforçant la circulation verticale, elle augmente le transport de la chaleur vers le nord, tandis qu'elle n'a aucun effet sur le transport de la salinité vers le nord. Il n'y a toutefois pas de différence qualitative très importante entre la circulation entraînée par les flux de salinité et de chaleur de surface et la circulation entraînée par ces deux flux et la force du vent. Alors que la présente étude, basée sur de nombreuses simplifications, n'a pas pour objet de simuler la circulation telle qu'elle est dans un océan réel, elle ne réussit pas à bien simuler la présence de la couche de salinité minimum, qui est une caractéristique commune à tous les océans. D'ailleurs, des courants de surface sont convergents d'une manière iréelle autour de 40°N au voisinage de la cote est.

1. Introduction

A previous paper (TAKANO, 1978), hereafter referred to as *T*, showed that an oversimplified equation of state for sea water as often used in numerical models of the ocean circulation leads to a result substantially different from a result obtained by a better approximate equation of state. Since the primary interest laid there in the role of the approximation to the equation of state, the ocean was driven by a thermal forcing only. Neither surface wind stress nor surface salinity flux was taken into account.

The purpose of the present study is to understand to what extent the general circulation in an ocean depends on a surface salinity flux, a surface heat flux and a surface momentum flux. A pioneering work by BRYAN and COX (1967) is alike in kind, but a very simple equation of state is used and the salinity is practically ignored.

2. Model

The basic equations and the boundary conditions are unless otherwise mentioned the same as the previous ones in *T*. The geometry of the ocean basin, the grid structure and the finite differencing schemes are also the same as those in *T*. Since these are described in *T*, only some of the principal features are presented here.

The ocean is bounded by two meridians 48° apart and by two parallels 70° apart. The southern boundary is on the equator. Symmetry is assumed with respect to the equator. The depth is 4000 m everywhere. The horizontal grid size is 2° in both longitude and latitude. The horizontal components of the velocity u and v, the temperature T and the salinity S are calculated at depths of 20, 120, 640, 1280 and 2760 m. The vertical component of the velocity w is calculated at depths of 70, 380, 960 and 2020 m. When such a coarse grid is used, the momentum advection becomes negligibly small, so that the momentum equations are linearized. The coefficient of horizontal diffusion is 2×10^8 cm^2 s^{-1} for the momentum and 2.5×10^7 cm^2 s^{-1} for both heat and salinity. The coefficient of vertical diffusion is 1.5 cm^2 s^{-1} for momentum,

* Received on August 31, 1981
** Institute of Biological Sciences, University of Tsukuba, Sakuramura, Ibarakiken, 305 Japan

heat and salinity.

There is no friction along the bottom and the southern boundary, no slip along the western, northern and eastern boundaries. There is neither heat flux nor salinity flux through the bottom and the lateral boundary.

Three cases are studied. In the first case, Case 1, the density varies as a linear function of salinity S

$$\rho=\rho_0(1+\gamma S)\,, \qquad (1)$$

where ρ_0 is a constant and γ is a constant, too, assumed to be 7×10^{-4}. It is a much better approximation to use a linear equation for the salinity dependency of the density than to use a linear equation for its temperature dependency, because γ in Eq. (1) does not largely depend on the salinity, while the coefficient of thermal expansion depends to a greater extent on the temperature.

Neither thermal forcing nor wind stress is applied to the ocean surface. The temperature is constant everywhere. Case 1 is concerned with a haline circulation.

The surface boundary conditions for the momentum and salinity are

$$\rho\kappa\frac{\partial}{\partial z}(u, v)=0\,, \qquad (2)$$

$$\kappa\frac{\partial S}{\partial z}=S(E-Pr)\,, \qquad (3)$$

where κ is the coefficient of vertical diffusion, z is the vertical coordinate, positive upward, E is the evaporation and Pr is the precipitation; $(E\text{-}Pr)$ is prescribed.

The second case, Case 2, is concerned with a thermohaline circulation. In addition to Conditions (2) and (3), the surface thermal condition is given, as in T, by

$$c\rho\kappa\frac{\partial T}{\partial z}=d(T_A-T_S)\,, \qquad (4)$$

where c is the specific heat, T_S is the calculated surface temperature, T_A is a prescribed reference atmospheric temperature and d is a constant, assumed to be $50\,\mathrm{cal\,cm^{-2}\,day^{-1}}$. No wind stress is given. The equation of state is a formula by

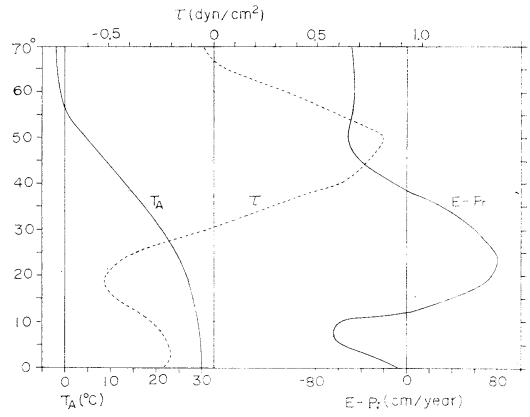

Fig. 1. External forcing $(E-Pr)$, T_A and τ.

FRIEDRICH and LEVITUS (1972), which determines the density as a function of temperature, salinity and pressure.

The last case, Case 3, deals with a thermohaline-wind-driven circulation. A wind stress is applied to Case 2. In place of Condition (2), we have

$$\rho\kappa\frac{\partial}{\partial z}(u, v)=(\tau, o)\,, \qquad (5)$$

where τ is the zonal component of the wind stress. There is no meridional component of the wind stress. Conditions (3) and (4) remain unchanged.

The external parameters $(E\text{-}Pr)$, T_A and τ are shown in Fig. 1. All is independent of the longitude; $(E\text{-}Pr)$ is the annual zonal mean of the precipitation minus evaporation over all the oceans, T_A is somewhat arbitrary and taken here to be identical with that used in Cases 2 and 3 in T, and τ is the annual zonal mean of the zonal stress over all the oceans estimated by HELLERMAN (1967, 1968).

The time integration is achieved as follows. In Case 1, starting from a motionless state of a uniform salinity of 35 ‰, it is continued up to 251 years with a time step of 8 hours. The salinity field at the end of the 60th year is taken as the initial salinity field for Case 2. The initial temperature field in Case 2 is the temperature field at the end of the 64th year in Case 1 in T where the density is calculated by a linear function of temperature. With the

formula by FRIEDRICH and LEVITUS, Case 2 starts from the initial state defined by these temperature and salinity fields and the geostrophic velocities calculated by them, and runs over about 112 years with a time step of 5 hours.

In Cases 1 and 2, the vertical integral of the horizontal velocity vanishes everywhere, because there are no wind stress, no depth change, no bottom friction, no momentum advection. In Case 3, however, subject to a wind forcing, the vertical integral of the horizontal velocity does not vanish any more. It is determined by the wind stress curl.

The vertical mean (barotropic component) of the velocity is decoupled from the shear current (baroclinic component). Although the vertical mean affects to a certain extent the shear current through the horizontal advection of the heat and salinity, there is no energy exchange between these two components of the velocity.

The vertical mean is obtained from the vorticity equation. Starting from the initial state where the planetary vorticity advection is balanced with the wind stress curl, the time integration is forwarded over 545 days with a time step of 12 hours. The velocity field averaged over the last 44 days is used as the vertical mean for Case 3.

Together with the vertical mean of the velocity obtained in this way, the shear current, temperature and salinity at the end of the 18th year in Case 2 are used as the initial state for Case 3. With the wind stress, the time integration is forwarded over 118 years with a time step of 5 hours. The total period of integration is 172 years in Case 2 and 190 years in Case 3.

The relaxation time of the whole ocean basin is so long that no steady state is reached in such a short time integration. At the end of the time integration, the overall mean salinity is increasing at a rate of 0.50×10^{-4} ‰ year^{-1} in Case 1, 0.16×10^{-3} ‰ year^{-1} in Case 2 and 0.12×10^{-4} ‰ year^{-1} in Case 3. The overall mean temperature is also increasing at a rate of 0.10×10^{-2}°C year^{-1} in Case 2 and -0.16×10^{-2}°C year^{-1} in Case 3. All these figures suggest that an almost, though not complete, steady state be reached in each case.

3. Velocity field

Case 1. Figure 2 shows the horizontal velocity distribution at a depth of 20 m. Three gyres spread over the whole ocean surface. Of them, the anticyclonic gyre in the tropics is strongest with a well developed western boundary current flowing northward. Its maximum speed is 7.6 cm s^{-1}. The anticyclonic gyre at high latitudes is weakest with a broad, not well defined western boundary current. As is seen in Fig. 1, the meridional gradient of $(E-Pr)$ is negative between the equator and 8°N, between 24°N and 50°N, and between 60°N and 70°N. It is positive in the remaining zonal belts. Subject to the boundary condition (3), the surface density tends to increase with $(E-Pr)$. Since the geostrophic relation should hold good, eastward currents develop at the surface layer in the zonal belt where $\frac{\partial}{\partial\varphi}(E-Pr)$ (φ: latitude) is positive, and westward currents develop at the surface layer in the zonal belt where $\frac{\partial}{\partial\varphi}(E-Pr)$ is negative. This gives rise to a three-gyre circulation as shown in Fig. 2. Because the absolute value of $\frac{\partial}{\partial\varphi}(E-Pr)$, either positive or negative, is small at middle and high latitudes, the resulting gyres are weak, whereas the strong

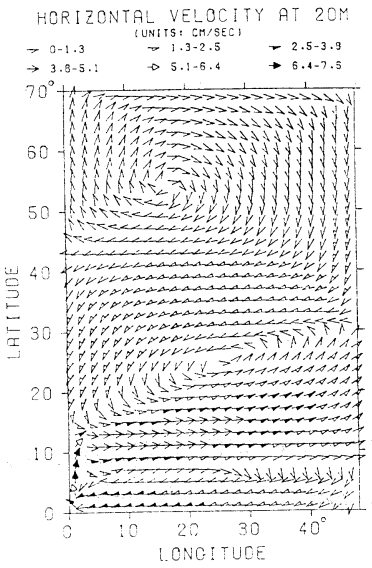

Fig. 2. Horizontal velocities at a depth of 20 m in Case 1.

tropical gyre results from the sharp gradient of $(E-Pr)$.

The circulation pattern at a depth of 120 m is similar to that at 20 m, though the motion is a little weaker. The maximum speed is decreased from 7.6 cm s^{-1} at 20 m to 6.4 cm s^{-1}.

At a depth of 640 m, the cyclonic gyre which is present at middle latitude upper layers is still persistent, but there is no well developed gyre at high latitudes. In this regard, a depth of 640 m might be considered as a transition layer from the upper layer motion to the lower layer motion, the former characterized by an anticyclonic gyre at high and low latitudes and a cyclonic gyre at middle latitudes, the latter characterized by a cyclonic gyre at high and low latitudes and an anticyclonic gyre at middle latitudes.

Figure 3 shows the velocity field at 1280 m. A cyclonic gyre is well developed at high latitudes. There is another cyclonic gyre, not so well organized but stronger, in the tropics. Middle latitude currents flow westward between these two cyclonic gyres.

At a depth of 2760 m a well organized anticyclonic gyre appears at middle latitudes. With a westward current at the equator, the circulation in the tropics is anticyclonic rather than cyclonic, while the high latitude gyre remains clearly cyclonic.

Case 2. Figure 4 shows the velocity field at 20 m. Comparison with Case 1 (Fig. 2) indicates that the surface heat flux and the surface salinity flux work so as to weaken the haline circulation and thermal circulation each other except in the tropics and in the central and eastern portion at low latitudes.

It might be remarked that the formulation in Case 2 in T, hereafter referred to as Case $2T$, is identical with that in Case 2 except for the salinity which is constant (35‰) everywhere in Case $2T$, but variable in the present Case 2. For comparison, the velocity field at 20 m in Case $2T$ is reproduced in Fig. 5. Figures 4 and 5 are different from each other in two regions, one is north of 57°N except in the eastern portion and the other is between 5°N and 21°N except in the eastern portion and near the western boundary. It is readily seen that the result in Case 2 is not merely a linear superposition of the result in Case 1 upon the result in Case $2T$ ([Fig. 4]≠[Fig. 2]+[Fig. 5]).

The motion is slower in Case 2 than in Case $2T$, indicating that the salinity variation weakens the circulation. The maximum speed is decreased from 25.7 cm s^{-1} in Case $2T$ to 22.0 cm

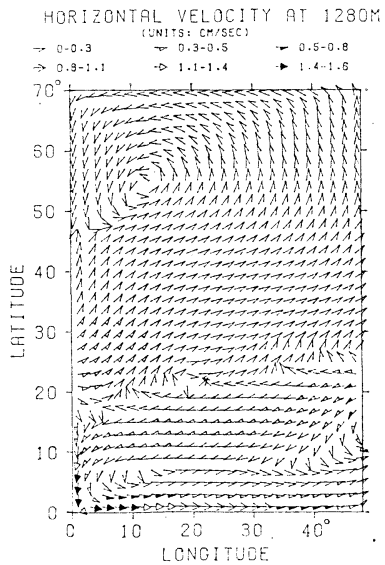

Fig. 3. Horizontal velocities at a depth of 1280 m in Case 1.

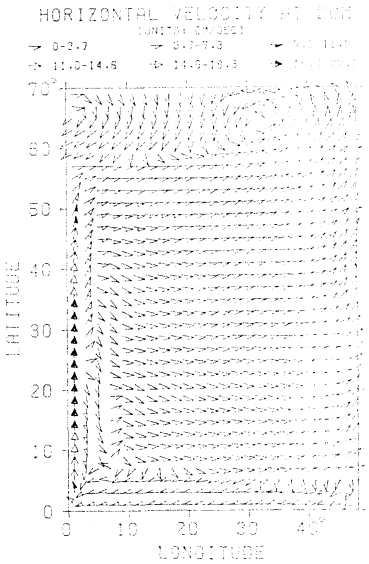

Fig. 4. Horizontal velocities at a depth of 20 m in Case 2.

s^{-1} in Case 2. The ratio of the total kinetic energy in the whole ocean basin in Case 2 to that in Case 2*T* is 1:1.40.

No significant qualitative difference is found between the circulation at 20 m and the circulation at 120 m, though the latter is a little weaker. The maximum speed is decreased from 22.0 cm s^{-1} at 20 m to 18.8 cm s^{-1} at 120 m.

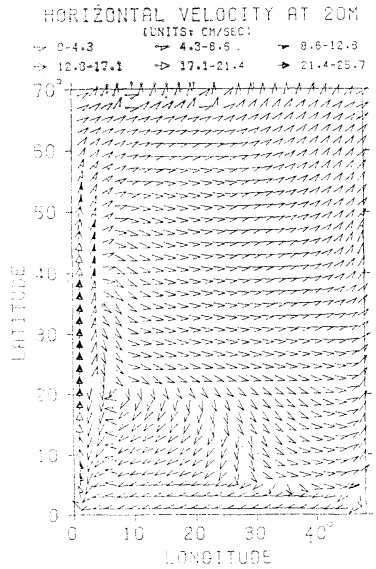

Fig. 5. Horizontal velocities at a depth of 20 m in Case 2*T*.

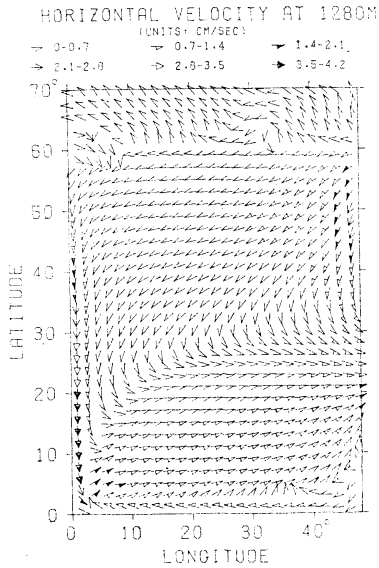

Fig. 6. Horizontal velocities at a depth of 1280 m in Case 2.

At 640 m, the equatorial current changes its direction to flow eastward. The western boundary current in the tropics also changes its direction and flows southward. Currents in the mid-ocean are predominantly westward at middle latitudes and eastward between 53°N and 59°N. North of 59°N, there is still a cyclonic gyre, similar to that at a depth of 20 m, though it is much weaker. The current pattern at this depth is similar to that in Case 2*T* except north of 61°N where the currents are predominantly eastward in Case 2*T*.

Figure 6 gives the velocity field at 1280 m. A large cyclonic gyre overspreads except near the equator and the eastern portion around 40°N. This pattern is similar to that in Case 2*T* shown in Fig. 7. The most significant qualitative difference between Case 2 and Case 2*T* is in the current direction at 1°N.

Comparison with the result in Case 2*T* shows that, except at 1°N at a depth of 1280 m, the effect of the salinity variation is pronounced north of 60°N only where the temperature is so low that the effect of its variation on the water density is small.

Three gyres appear at 2760 m; a well organized gyre at high latitudes, another anticyclonic gyre

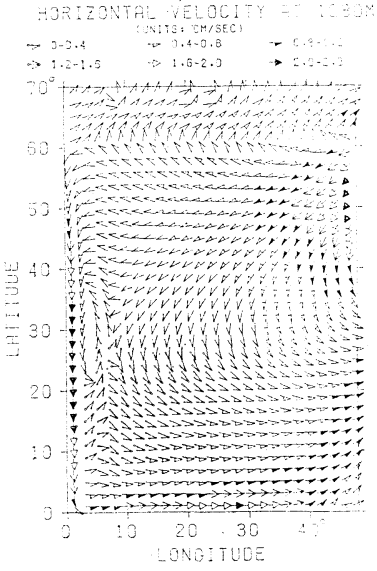

Fig. 7. Horizontal velocities at a depth of 1280 m in Case 2*T*.

in the tropics and a cyclonic gyre at middle latitudes. The pattern in Case *2T* is much simpler. It is rather a single cyclonic gyre pattern with its center at 33°N.

Case 3. Figure 8 gives the vertical mean of the velocity obtained from the vorticity equation as mentioned above, which exclusively depends on the wind stress curl. The wind stress curl vanishes at three latitudes, around 4°N, 18°N and 48°N. Four gyres, separated by these three parallels, are correspondingly developed. The western boundary current flows at a maxi-

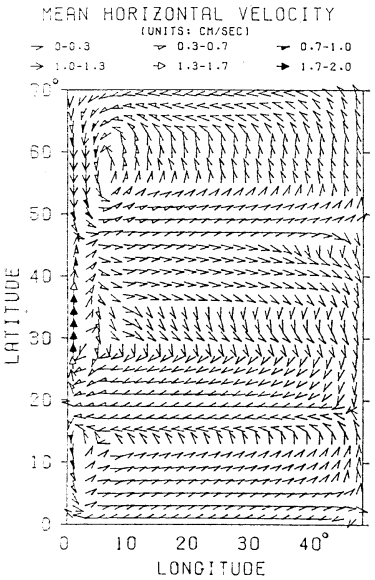

Fig. 8. Vertical mean of the horizontal velocity in Case 3.

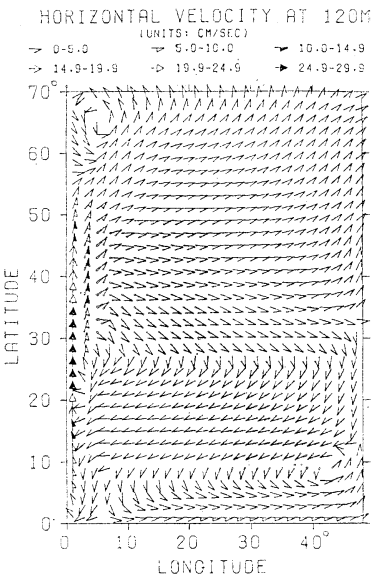

Fig. 10. Horizontal velocities at a depth of 120 m in Case 3.

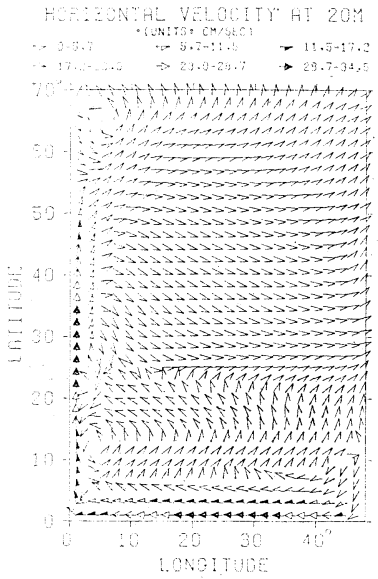

Fig. 9. Horizontal velocities at a depth of 20 m in Case 3.

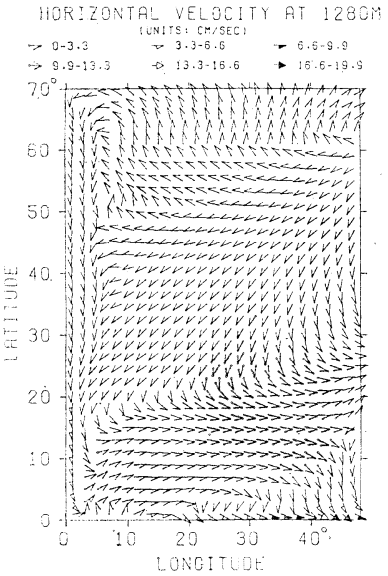

Fig. 11. Horizontal velocities at a depth of 1280 m in Case 3.

mum speed of 2.0 cm s^{-1}. The transport of the western boundary current is 15.7×10^{12} cm^3 s^{-1}. This small transport results from the small longitudinal extent of the ocean basin and from the large coefficient of horizontal eddy diffusion which in turn results from the coarse grid size.

Figures 9, 10 and 11 show the velocity field at 20, 120 and 1280 m. Although Cases 1, 2 and 2*T* indicate no significant difference between the velocities at 20 m and those at 120 m in each case, Case 3 is another thing in two respects. First, due to the surface wind stress, the 20 m layer is much more active than the 120 m layer. Secondly, the surface Ekman layer, though not well resolved by the coarse grid used here, makes the current pattern quite different from each other south of 25°N except for the northward flowing western boundary current. The equatorial current flows westward at 20 m but eastward at 120 m, certainly related to the equatorial undercurrent, though not well resolved by the poor vertical resolution. North of the equatorial current, currents flow northeast to north at 20 m but south to southwest at 120 m.

The surface circulation is different from that in Case 2 in two respects. First, currents flow much faster everywhere. The maximum speed is increased from 5.1 cm s^{-1} to 30.9 cm s^{-1} for the equatorial current, and from 21.9 cm s^{-1} to 32.7 cm s^{-1} for the western boundary current. So is the circulation at 120 m, too. The maximum speed of the equatorial current is increased from 2.1 cm s^{-1} to 7.2 cm s^{-1} and its direction is opposite to that in Case 2. The speed of the western boundary current is increased from 18.8 cm s^{-1} to 28.0 cm s^{-1}. Secondly, the high latitude cyclonic gyre is shifted to the east and enlarged to the south. Its southern boundary lies on about 50°N instead of 55°N in Case 2.

Hence, the wind-driven, thermohaline circulation is much stronger than the thermohaline circulation. The total kinetic energy of the baroclinic component of the velocity in Case 3 is 3.21 times as large as that in Case 2.

At 640 m, the currents are generally weak, and meridional rather than zonal. The western boundary current is correspondingly not well organized. It is directed southward in the tropics. The equatorial current flows westward at the eastern half.

At 1280 m, the western boundary current is broad, though more distinctly defined than at 640 m, and flows southward all along the boundary. The equatorial current changes again its direction. The overall pattern is not significantly different from that in Case 2 except in the eastern half of the equatorial region where the current direction is reverse and except in the northwestern corner where a small cyclonic gyre is present in Case 3.

At 2760 m, the western boundary current still flows southward almost all along the boundary. What is peculiar to Case 3 is that the western boundary current at high latitudes north of 50°N flows southward from the surface down to the bottom. The equatorial current is predominantly westward. The frequent reverse of its direction with increasing depth is another peculiarity in Case 3.

4. Salinity field

Case 1. Figure 12 shows the salinity field at 120 m, which is almost identical with the salinity

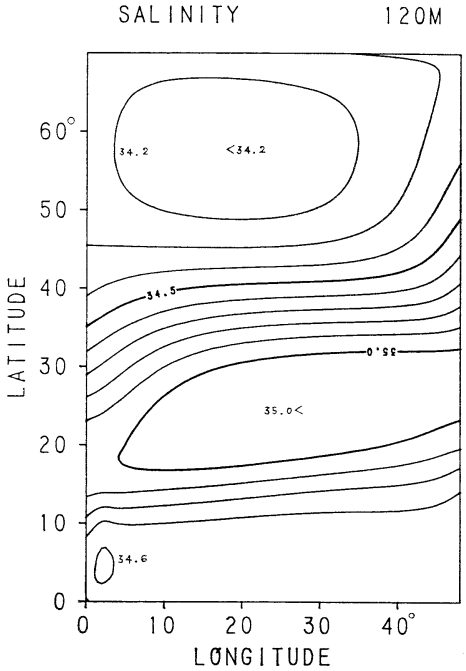

Fig. 12. Salinity at 120 m in Case 1. Contour interval: 0.1 ‰.

field at 20 m. Because the water density is determined by the salinity alone, the vertical stratification at the surface is stable or unstable according as $(E-Pr)$ is negative or positive. Then, a strong vertical mixing takes place in upper layers between 12°N and 38.5°N where $(E-Pr)$ is positive so as to restore a stable stratification. Therefore, the positive $(E-Pr)$ increases not only the salinity at a shallow surface layer but also the salinity at deeper layers by the haline convection. The surface salinity is consequently not readily increased, whereas it is readily decreased wherever $(E-Pr)$ is negative because of absence of the haline convection.

The southward pushing of isohalines near the western boundary between 23°N and 40°N results from the southward advection of low salinity water by the southward boundary current. It is also the case with the slight northward pushing near the eastern boundary between 12°N and 22°N. The boundary current flows northward there. However, the northward pushing near the eastern boundary between 35°N and 55°N is another thing. The boundary current is not northward but southward there. No horizontal advection can account for it. Instead, an upwelling brings a deep saline water mass from a depth of 380 m which in turn originates by sinking from the surface layer resulting from a large positive $(E-Pr)$ to the south. The maximum upward speed is about 10^{-2} cm s^{-1}.

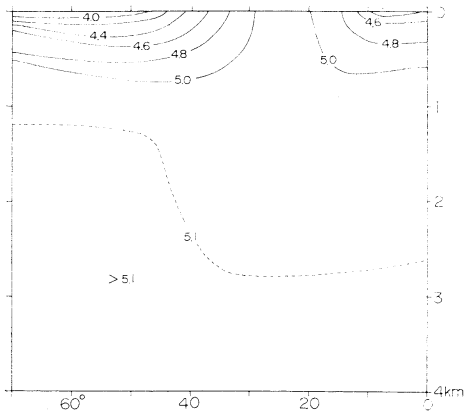

Fig. 13. Zonal average of the salinity in Case 1. Numbers refer to (S-30 ‰).

The salinity at 640 m varies with longitude rather than latitude. It is low at the eastern boundary region in the tropics and at the western boundary region at middle latitudes, while it is high at the western boundary region in the tropics and at the eastern boundary region at high latitudes. To the contrary, the salinity at 1280 m and 2760 m is increased with latitude with exception of a few limited areas in the eastern and western boundary regions.

The zonal average is shown in Fig. 13. Isohalines clearly reflects the formation and downward spreading of the most saline water mass between 20°N and 30°N, and the formation of low salinity waters at high latitudes. The density depending on the salinity only, the salinity is monotonically increased with depth to keep the stable stratification.

Case 2. So far as the vertical stratification is concerned, the temperature works as a stabilizer by surface heating at low and middle latitudes where (T_A-T_S) is positive, and as a destabilizer by surface cooling at high latitudes where (T_A-T_S) is negative. The difference (T_A-T_S) is

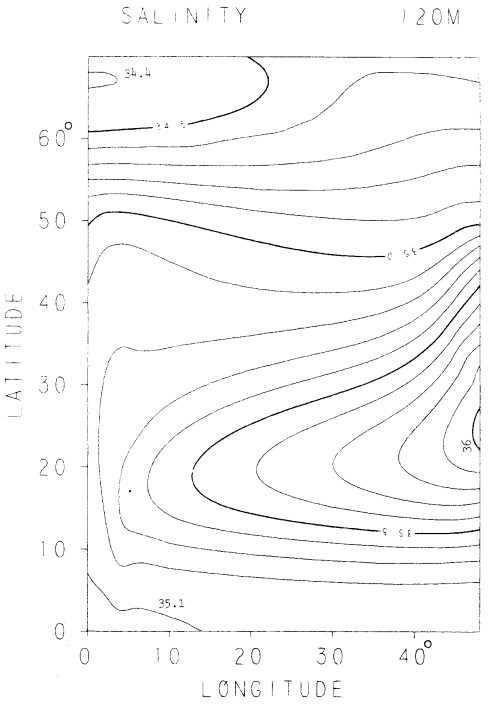

Fig. 14. Salinity at 120 m in Case 2. Contour interval: 0.1 ‰.

mostly positive between 12°N and 38.5°N where saline waters are formed as is seen in Case 1. Therefore, the stabilization by heating does not allow the surface saline water to sink into deeper layers so readily as in Case 1. Then, the surface salinity is increased. The maximum surface salinity becomes 36.51 ‰ compared with 35.09 ‰ obtained in Case 1. The minimum salinity, 34.13 ‰, becomes higher in a similar way than the minimum, 33.81 ‰, in Case 1.

The isohalines at 20 m and 120 m (Fig. 14) are alike in general configuration. A strong sinking of the order of 10^{-3} cm s^{-1} at a depth of 70 m brings about the surface saline water to the eastern portion between 20°N and 40°N. The maximum salinity at this level, 36.03 ‰, is found there. To the north, associated with strong convergence of surface currents, sharp meridional gradients are formed around 40°N.

The isohaline pattern at 640 m is not very different from that at 120 m. At middle latitudes a tongue-like saline water mass extends from the eastern boundary far to the west. At high latitudes the salinity varies very little with longitude.

Figure 15 shows that a saline water mass spreads almost uniformly far to the western boundary at 1280 m. The salinity is decreased with latitude in the greater part of the ocean basin. Sharp gradients are seen in the northeastern corner. It might be noted that in Case 1 the salinity is increased with latitude at depths of 1280 m and 2760 m.

At 2760 m, the lowest salinity, 34.98 ‰, is present at 30°N on the eastern boundary. The salinity is increased to the north and to the northwest.

The zonal average is shown in Fig. 16. Reflecting the meridional overturning governed by the temperature rather than the salinity as shown later in Fig. 30, the low salinity water mass formed at high latitudes is not confined into upper layers any more, which presents a striking contrast to Case 1. It spreads deeper and to the south. Instead, the saline water mass is confined into upper layers around 20°N.

Case 3. The Ekman drift is convergent in zonal belts ranging from the equator to 11°N and from 15°N to 43°N, while it is divergent from 11°N to 15°N and from 43°N to 70°N. The resulting vertical motion at the bottom of the Ekman frictional layer is downward from the equator to 11°N, and from 15°N to 43°N, upward from 11°N to 15°N, and from 43°N to 70°N. As seen in Cases 1 and 2, the most saline surface water is formed at the eastern boundary around 24°N where $(E-Pr)$ is largest. The vertical motion due to the wind stress is

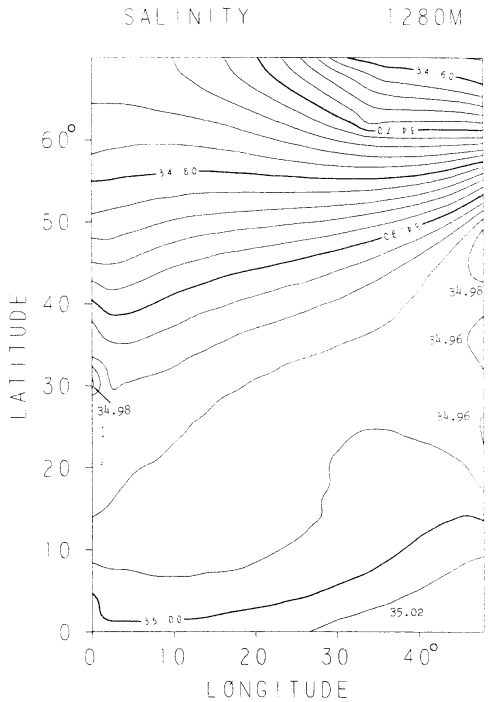

Fig. 15. Salinity at 1280 m in Case 2. Contour interval: 0.02 ‰.

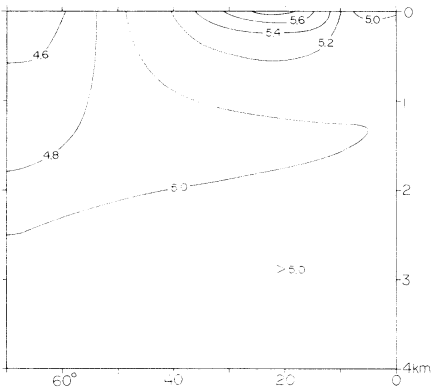

Fig. 16. Zonal average of the salinity in Case 2. Numbers refer to (S-30 ‰).

downward at the bottom of the Ekman frictional layer in this zonal belt. Hence, the wind stress tends to accelerate the sinking of the surface water in this belt which is weakened by the thermal stabilizing effect. Compared with Case 2, the highest surface salinity is decreased in this way. It is 36.40‰, lower by 0.11‰ than in Case 2.

Due to the high latitude upwelling of saline deep water resulting from the Ekman divergence, the high latitude lowest salinity is increased up to 34.97‰, higher by 0.84‰ than in Case 2.

Figure 17 gives the zonal mean of the surface salinity in the three cases together with the prescribed (*E-Pr*). The zonal mean is closely related to (*E-Pr*) in all the cases. For the reason mentioned above, the thermal forcing increases the surface salinity considerably. North of 22°N and south of 5°N, the wind stress makes the surface salinity higher than in Case 2. Its effect is more pronounced at high latitudes. The latitude where the salinity becomes maximum depends on the direction of the meridional component of the currents at 2°~30°N; it is directed southward (Fig. 4) in Case 2 and northward (Fig. 9) in Case 3.

The salinity at 120 m is shown in Fig. 18. Although the isohaline pattern resembles that in Case 2, the salinity is slightly lower around 24°N at the eastern boundary and higher at high latitudes. These features are also seen at 20 m.

A remarkable contrast between Cases 2 and 3 is found in the salinity range on the equator.

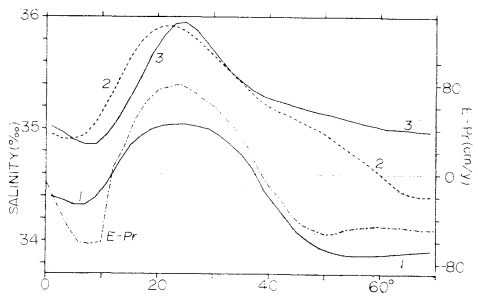

Fig. 17. Surface salinities in Cases 1, 2 and 3, and (*E-Pr*).

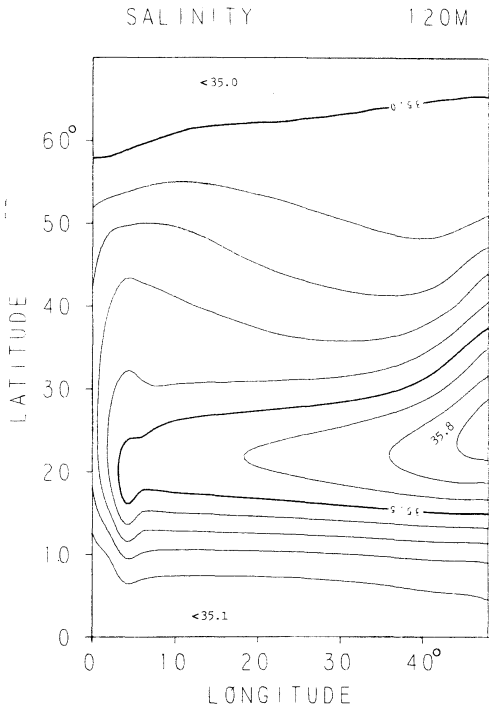

Fig. 18. Salinity at 120 m in Case 3. Contour interval: 0.1‰.

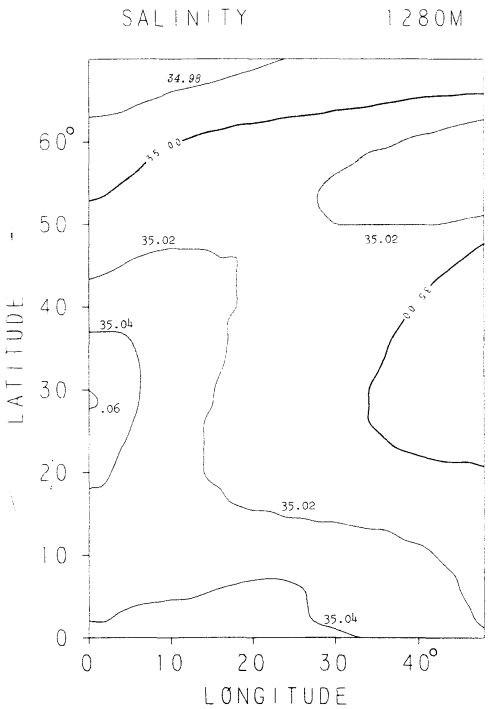

Fig. 19. Salinity at 1280 m in Case 3. Contour interval: 0.02‰.

The difference between the maximum and the minimum at the surface is 0.08‰ in Case 3 in place of 0.02‰ in Case 2. This contrast, more striking in the temperature, results from the wind stress as mentioned later. The difference at 640 m is 0.03‰ in Case 3 against 0.01‰ in Case 2.

Due to the much stronger western boundary current than in Case 2, isohalines at 120 m are pushed northward more clearly at middle latitudes and southward at high latitudes.

The isohalines at 1280 m (Fig. 19) are not so distinctly zonal as those in Case 2. Further, the salinity is horizontally much more uniform than in Case 2.

The 2760 m isohalines run in the zonal direction rather than in the meridional direction, while they are rather meridional in Case 2.

Figure 20 shows the zonal mean. The wind stress extends the upper saline water mass to the north. Compared with Case 2, the high latitude sinking into deeper layers suppresses the tongue-like southward extension of low salinity waters in intermediate depths which is peculiar to Case 2. The salinity minimum layer, present between 1000 m and 2000 m in Case 2, disappears in this way.

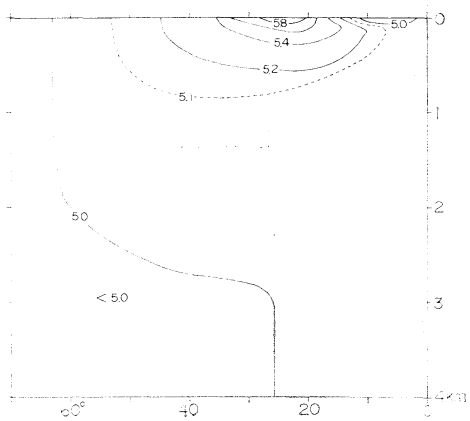

Fig. 20. Zonal average of the salinity in Case 3. Numbers refer to (S-30‰).

Table 1. Mean salinities (‰)

Depth (m)	Case 1	Case 2	Case 3
20	34.49	35.25	35.29
120	34.65	35.22	35.28
640	35.01	35.01	35.09
1280	35.08	34.93	35.02
2760	35.10	35.08	35.01
Average	35.038	35.041	35.047

Table 1 tabulates the mean salinities at the five levels and the salinities averaged over the whole ocean basin.

While the mean salinity is monotonically increased with depth in Case 1 and decreased with depth in Case 3, it becomes minimum at an intermediate depth in Case 2. With the wind stress, no salinity minimum layer exists, which is in disagreement with the observation. Another marked disagreement with the observation is in the horizontal distribution. The observed salinity field shows no tongue-like pattern extending westward from the eastern boundary at middle latitudes. A high salinity area in upper layers is located in the mid-ocean in the North and South Pacific and the North Atlantic. There is a tongue-like pattern in the South Atlantic, but it extends from the western boundary, not from the eastern boundary.

5. Temperature field

Case 2. Figures 21 and 22 give the temper-

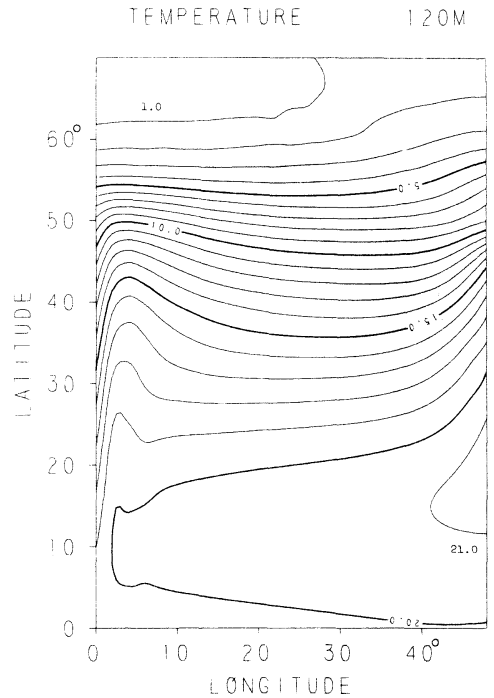

Fig. 21. Temperature at 120 m in Case 2. Contour interval: 1°C.

atures at 120 m in Cases 2 and 2*T*. While isotherms are crowded around 50°N near the eastern boundary in Case 2*T*, they are crowded around 40°N, lower by about 10°, in Case 2, due to southward currents at 20 m, 120 m and 640 m which the haline circulation produces along the eastern boundary at middle and high latitudes.

The temperature at low latitudes is higher in Case 2 by up to about 1°C than in Case 2*T*. Although this is also the case with the temperature at 20 m, the difference between Cases 2 and 2*T* is smaller (<0.5°C), because the surface layer is firmly governed by the prescribed reference atmospheric temperature. Higher surface temperatures in Case 2 should result from a weaker low latitude upwelling as shown later.

The temperature at high latitudes at 20 m and 120 m is lower in Case 2 than in Case 2*T*. This temperature difference should be interpreted as follows. In Case 2*T* a deep convection penetrates from the surface down to the bottom at high latitudes with downward motion along the northern boundary. On the contrary, in Case 2 where the salinity works so as to decrease the surface water density, the high latitude convection is confined into a much shallower layer with upward motion along the northern boundary. The cooling is therefore stronger than in Case 2*T*.

Figure 23 gives the temperature at 640 m. A sharp eastward increase in the western

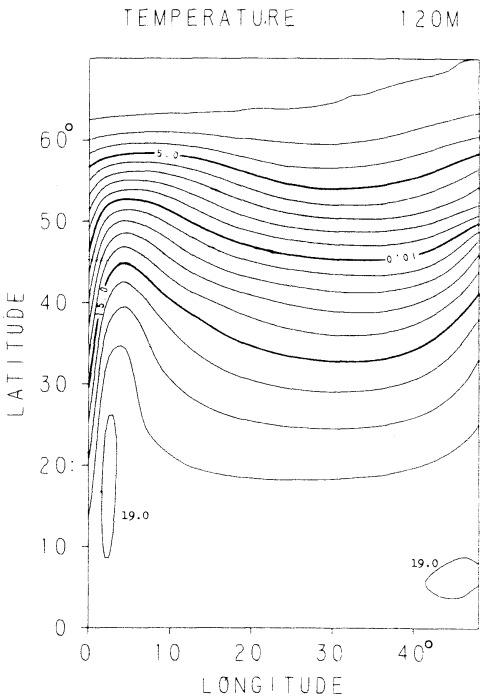

Fig. 22. Temperature at 120 m in Cose 2*T*
Contour interval: 1°C.

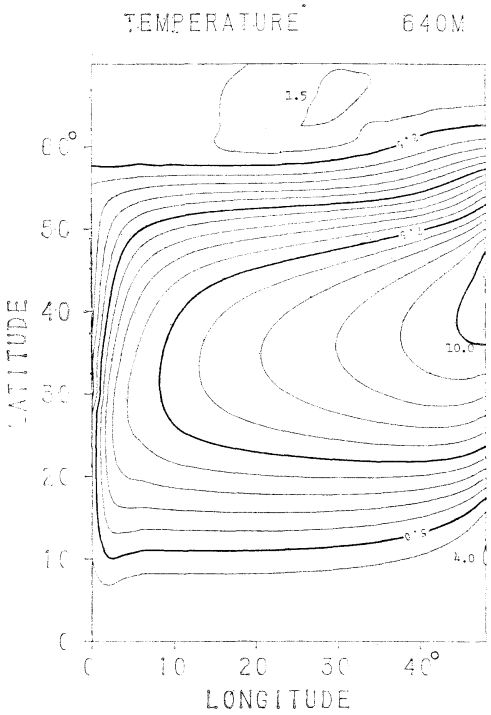

Fig. 23. Temperature at 640 m in Case 2.
Contour interval: 0.5°C.

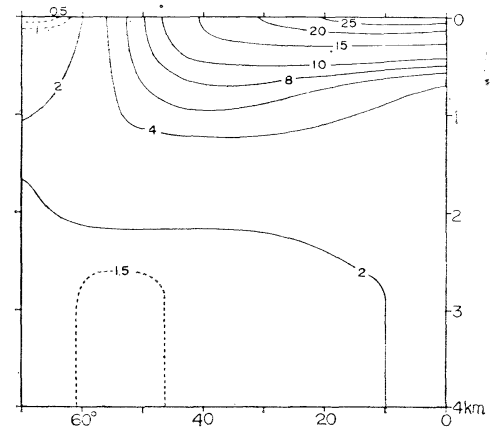

Fig. 24. Zonal average of the temperature in Case 2.

boundary region is closely related to the northward boundary current whose speed is $2\,\mathrm{cm\,s^{-1}}$ or less.

At middle latitudes a warm tongue-like core extends westward from the eastern boundary.

At 1280 m and 2760 m no sharp gradients are present in the western boundary region, whereas the eastern warm core is persistent around 50°N near the eastern boundary.

The zonal mean is figured in Fig. 24 for Case 2 and in Fig. 25 for Case 2*T*. In contrast with Fig. 25, Fig. 24 reveals warming at low latitudes subsurface layers and cooling at high latitudes due to the salinity variation.

Case 3. The temperature field in Case 3 is not significantly different from that in Case 2. The only remarkable difference is in the equatorial surface temperature. In Case 2, the surface temperature varies very little with longitude except in the vicinity of the western and eastern boundary where isotherms push slightly northward. It ranges from 27.54°C to 27.73°C at the equator. However, in Case 3 it is much more variable with longitude; 28.75°C in the west and 21.66°C in the east at the equator. This wide range arises from the wind stress. The Ekman drift turns out an upwelling of $2\times10^{-3}\,\mathrm{cm\,s^{-1}}$ in the eastern half, which decreases the surface temperature. In Case 2, the vertical velocity is upward, but of the order of $10^{-4}\,\mathrm{cm\,s^{-1}}$ or less, at the equator, at least one order of magnitude less than in Case 3.

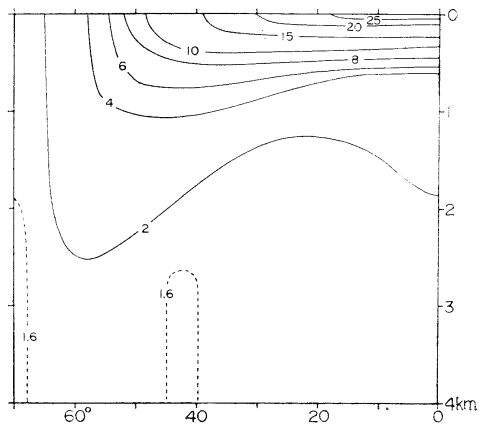

Fig. 25. Zonal average of the temperature in Case 2*T*.

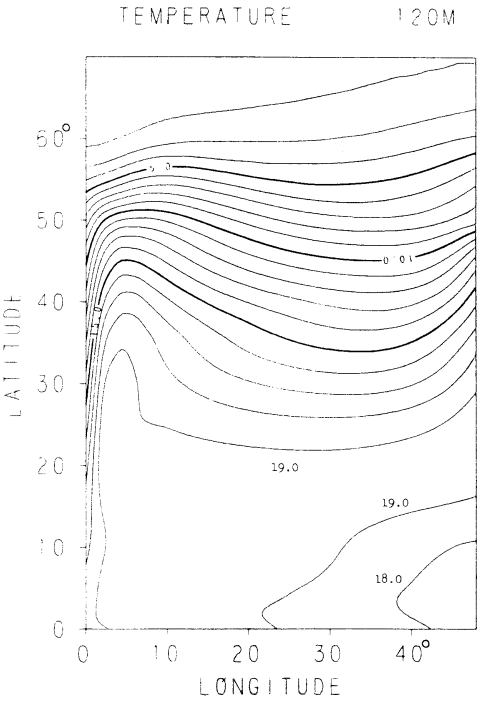

Fig. 26. Temperature at 120 m in Case 3. Contour interval: 1°C.

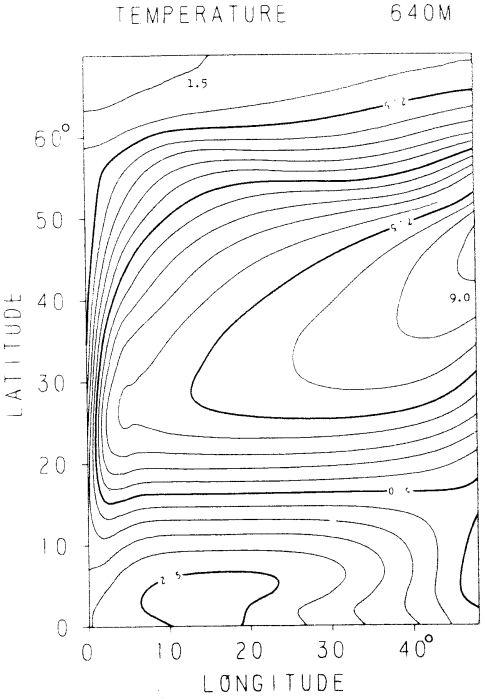

Fig. 27. Temperature at 640 m in Case 3. Contour interval: 0.5°C.

This difference between Cases 2 and 3 is not so pronounced at 120 m as at 20 m, as shown in Fig. 26 to be compared with Fig. 21.

Figure 27 shows the temperature field at 640 m. Compared with Case 2 (Fig. 23), the temperature in the eastern tropics varies with longitude rather than latitude. Related to the intensified boundary current, the horizontal thermal gradient at middle latitudes along the western boundary becomes sharper than in Case 2. Except for these two respects, the difference between Cases 2 and 3 is almost negligible. It is further smaller at 1280 m and 2760 m.

The zonal mean is shown in Fig. 28. The isotherm pattern is closer to that in Case 2*T* than to that in Case 2. Compared with Case 2*T*, however, isotherms above 4°C are pushed up to make a sharper thermocline at low and middle latitudes; in other words, comparison with Case 2 (Fig. 24) demonstrates the effect of the wind stress cooling low and middle latitude subsurface layers and warming high latitude surface layers.

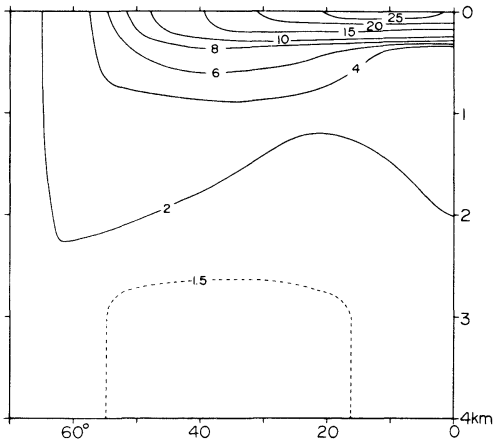

Fig. 28. Zonal average of the temperature in Case 3.

Table 2. Mean temperatures (°C)

Depth (m)	Case 2T	Case 2	Case 3
20	18.54	18.44	18.50
120	14.38	15.14	14.78
640	4.39	5.94	5.30
1280	2.16	2.74	2.20
2760	1.76	1.74	1.53
Average	3.52	3.94	3.58

The mean temperatures at the five levels in Cases 2*T*, 2 and 3 are tabulated in Table 2. The wind stress warms a little the top layer but cools lower layers, and increases the overall vertical stability.

6. Total meridional circulation

Integration of the equation of continuity from the western boundary to the eastern boundary gives

$$\frac{1}{R}\frac{\partial}{\partial\varphi}\int v\cos\varphi\, d\lambda+\frac{\partial}{\partial z}\int w\cos\varphi\, dz=0,$$

where w is the vertical component of the velocity, λ the longitude and R the earth's radius.

The transport stream function Φ for the meridional circulation integrated over the zonal extent of the ocean basin is defined by

$$\int vR\cos\varphi\, d\lambda=-\frac{\partial\Phi}{\partial z},$$

$$\int wR\cos\varphi\, d\lambda=\frac{1}{R}\frac{\partial\Phi}{\partial\varphi}.$$

Case 1. Figure 29 shows the meridional circulation in Case 1. The sinking region between 11°N and 31°N coincides fairly well with the zonal belt between 12°N and 38°N where $(E-Pr)$ is positive. Two main gyres, one clockwise and the other counterclockwise, are confined into upper layers. The former is centered at 31°N, 960 m, and transports −7.3 sv. The latter is centered at 11°N, 380 m, and trans-

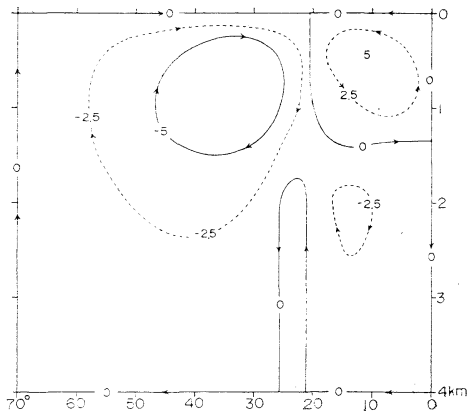

Fig. 29. Total meridional circulation in Case 1. Units: sv.

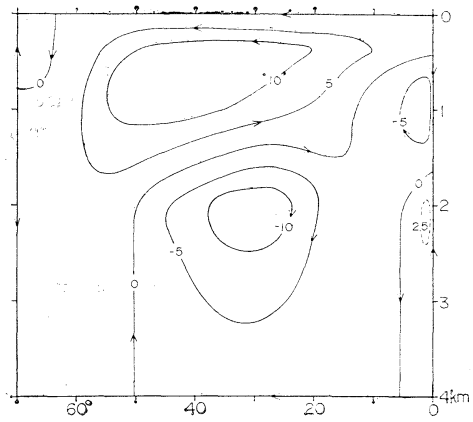

Fig. 30. Total meridional circulation in Case 2. Units: sv.

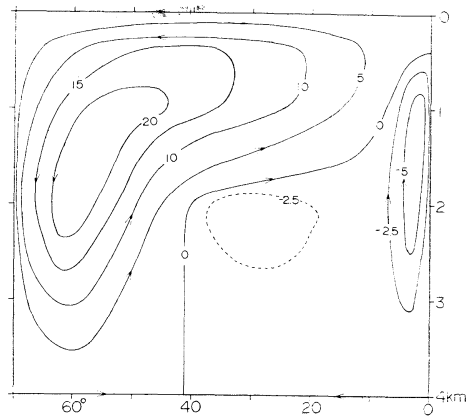

Fig. 31. Total meridional circulation in Case 2T. Units: sv.

ports 5.0 sv. Its shallowness relative to the former could be interpreted by a shorter space scale variation of $(E-Pr)$ between the equator and 20°N. Other two small gyres, located at low latitude deep layers transport -3.2 sv and 0.6 sv, respectively.

Case 2. Figure 30 refers to Case 2. Figure 31 is reproduced for Case 2T. Compared with Case 2T, the high latitude sinking is weakened and does not penetrate into deep layers. Its area is shifted to the south. The wane of the meridional circulation by the weak high latitude sinking results from the stabilizing effect of the low surface salinity at high latitudes.

The transport of the upper main gyre is decreased from 24 sv in Case 2T to 14 sv, while

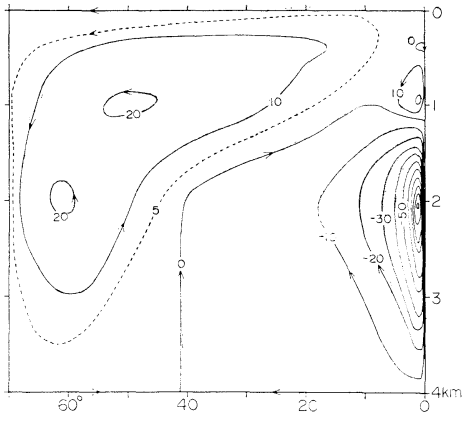

Fig. 32. Total meridional circulation in Case 3. Units: sv.

the transport of the deep gyre is increased from 3.8 sv to 13 sv.

Case 3. As is seen in Fig. 32, the application of the wind stress to Case 2 suppresses the weak upwelling along the upper northern boundary, enlarges and intensifies the upper gyre, which transports 21.3 sv. It also brings about an equatorward intensification of the deep central gyre. The strong sinking along the deep southern boundary is mainly due to the sinking at the eastern half of the equator.

7. Total zonal circulation

Integrated with respect to the latitude from the southern boundary to the northern boundary, the equation of continuity yields

$$\frac{1}{R}\frac{\partial}{\partial\lambda}\int u\,d\varphi+\frac{\partial}{\partial z}\int w\cos\varphi\,d\varphi=0\,.$$

The transport stream function Φ' is defined, as a measure of the total zonal circulation, by

$$\int uR\,d\varphi=-\frac{\partial\Phi'}{\partial z},$$

$$\int wR\,d\varphi=\frac{1}{R\cos\varphi}\frac{\partial\Phi'}{\partial\lambda}.$$

Case 1. Figure 33 shows the zonal circulation in Case 1. A large clockwise gyre spreads almost all over the whole domain and a small counterclockwise gyre occupies the upper western corner. The upper western boundary region is a sinking region. The former transports

9.1 sv and the latter 4.6 sv. The zonal circulation is stronger than the meridional circulation which transports 7.3 sv.

Case 2. Figure 34 refers to Case 2. A clockwise gyre develops over the whole upper layer 1000 m deep with a strong sinking in the eastern boundary region and a fairly strong upwelling in the western boundary region. Its transport is 19.8 sv, about 1.3 times as large as the transport of the meridional circulation (Fig. 30). For comparison, the zonal circulation in Case 2*T* is reproduced in Fig. 35. The introduction of the salinity variation considerably weakens both upper gyre and lower eastern gyre. Without salinity variation, the upper clockwise gyre transports 24.1 sv and the lower eastern gyre transports 28.7 sv, and the western boundary is an upwelling region from the surface to the bottom. The zonal circulation is as intense as the meridional circulation (Fig. 31).

Case 3. Figure 36 shows the zonal circulation in Case 3. Compared with Case 2, the trans-

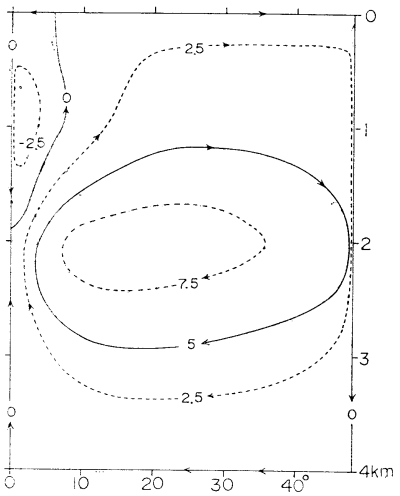

Fig. 33. Total zonal circulation in Case 1. Units: sv.

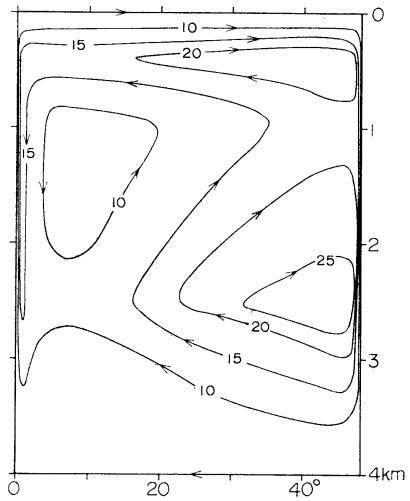

Fig. 35. Total zonal circulation in Case 2*T*. Units: sv.

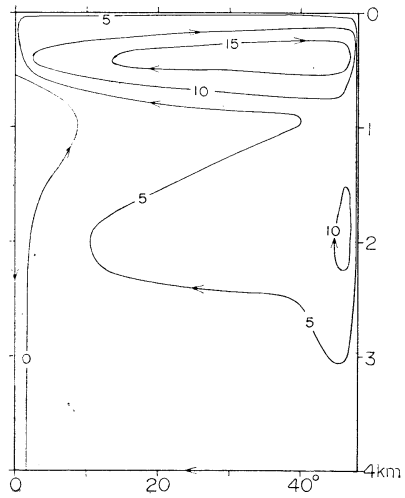

Fig. 34. Total zonal circulation in Case 2. Units: sv.

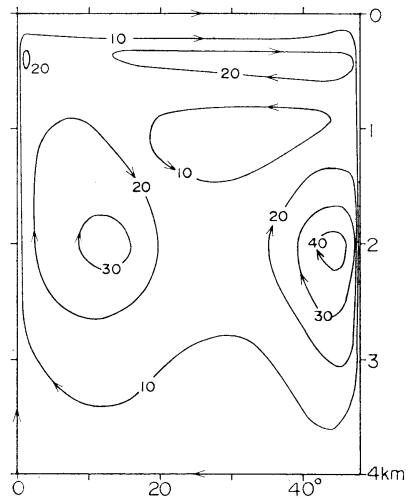

Fig. 36. Total zonal circulation in Case 3. Units: sv.

port of the upper clockwise gyre is a little increased from 19.8 sv to 24.7 sv. A wide-spread clockwise gyre of 35.2 sv appears in the deep western half, while another clockwise gyre of 44.6 sv is in the deep eastern half. The circulation is, therefore, clockwise in the whole domain.

8. Meridional salinity transport

The northward salinity transport across a latitude circle is achieved by the total meridional circulation, the total horizontal circulation and the subgrid scale eddy diffusion. The first gives rise to the net northward salinity transport by bringing surface waters northward and deep waters southward, both waters having different salinities. The second brings western boundary waters northward and central and eastern region waters southward, both waters having different salinities, which turns out a net meridional salinity transport. The third brings salinity from saline waters to less saline waters by diffusion. The sum of these three components is the total meridional transport.

Figure 37 gives the total transport in the three cases. As is readily seen from the distribution of $(E\text{-}Pr)$, there are two salinity sinks, north of 38°N and south of 12°N, and a salinity source between 12°N and 38°N. The salinity transport is correspondingly southward south of 22°~23°N with its maximum around 11°N, and northward north of 22°~23°N with its maximum around 38°N. Since the surface salinity flux is proportional to the surface salinity, which is lowest in Case 1, the sink and source are weakest in Case 1. Roughly speaking, Case 1 transports, therefore, the smallest amount of

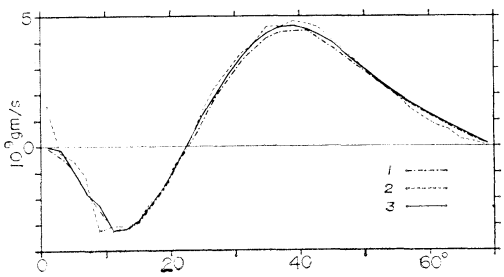

Fig. 37. Total meridional salinity transport. Numbers 1, 2 and 3 refer to Cases 1, 2 and 3, respectively.

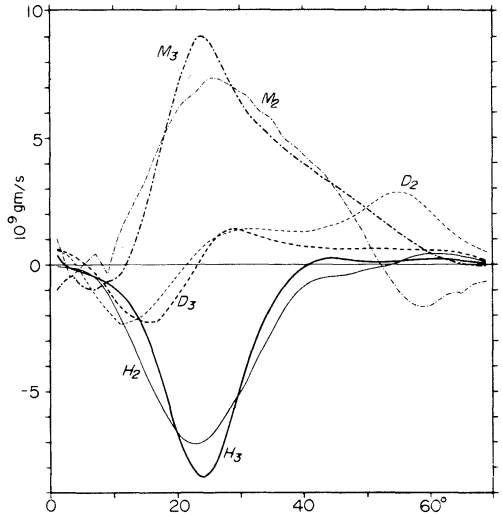

Fig. 38. Meridional salinity transports in Cases 2 and 3. Symbols M, H and D refer to the transports by the total meridional circulation, total horizontal circulation and subgrid scale eddy diffusion. Subscripts 2 and 3 refer to Cases 2 and 3, respectively.

salinity, though the difference between Case 1 and Cases 2 or 3 is very small.

Although the total transport at a given latitude circle is almost equal to each other in the three cases, the relative importance of each of the three components is not so. In Case 1, the meridional circulation is most important. Except between 20°N and 36°N, the transport by the horizontal circulation is almost negligible and much smaller than the transport by eddy diffusion.

Figure 38 shows the three components in Cases 2 and 3. The salinity is mostly transported northward by the meridional circulation and southward by the horizontal circulation. The transports by both circulations are almost cancelled out each other. In Case 3 at high latitudes the northward transport by the meridional circulation is increased and the northward transport by the eddy diffusion is decreased.

9. Meridional heat transport

Just as the meridional salinity transport, the meridional heat transport is achieved by the total meridional circulation, the total horizontal circulation and the subgrid scale eddy diffusion.

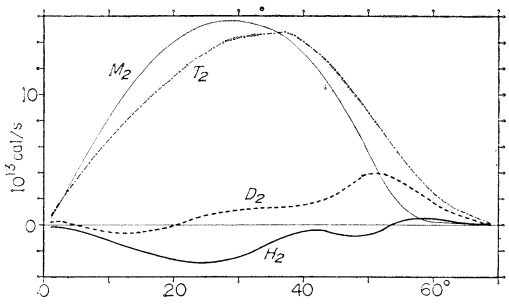

Fig. 39. Meridional heat transport in Case 2. Symbols T, M, H and D refer to the total transport, to the transports by the meridional circulation, horizontal circulation and eddy diffusion.

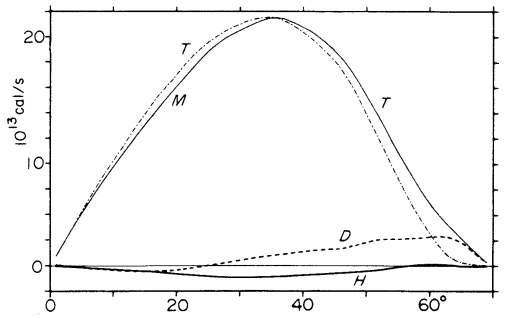

Fig. 40. Meridional heat transport in Case $2T$.

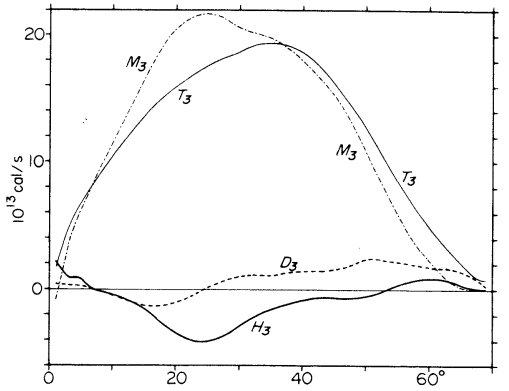

Fig. 41. Meridional heat transport in Case 3.

Figures 39 to 41 show the transport by each of them and the total transport in Cases 2, $2T$ and 3. In all the cases, the meridional circulation is of the greatest importance. Its transport is northward almost all over the latitude circles. Contrary to the salinity transport, the horizontal circulation is of minor importance. Its transport is southward except at high latitudes. In Case 3, associated with the northward Ekman drift by the wind stress, the transport by the horizontal circulation is northward in a narrow zonal belt south of 5°N. As in the salinity transport, the importance of the subgrid scale eddy diffusion relative to the other two components is increased at high latitudes. Compared with Case 2, the wind stress increases by about 20 % the transport by the meridional circulation as well as the transport by the horizontal circulation.

10. Summary and discussion

The above results are summarized as follows.

(1) The surface salinity flux weakens the circulation in the greater part of the ocean basin by working opposite to the thermal and momentum forcing.

(2) However, the overall effect of the salinity is not so pronounced that the results in Case 2 and Case $2T$ are almost alike except in a few respects such as general wane of the current velocities and of the total meridional circulation, general warming of deep waters, particularly at intermediate depths.

(3) In any case, surface currents converge at 40~50°N near the eastern boundary. The convergence is particularly strong in the case of the uniform salinity (Case $2T$), which brings a lot of cold surface waters to deeper layers.

(4) The wind stress increases the current velocities as a whole, decreases the temperature averaged over the whole ocean basin, but increases the surface temperatures, intensifies the total zonal circulation as well as the total meridional circulation, increases the total meridional heat transport, but does not affect the total meridional salinity transport.

(5) Although the salinity averaged over the whole ocean basin is not significantly different from each other in the three cases, its vertical distribution is not so. The average surface salinity is especially low in Case 1. In Case 2 only a salinity minimum layer exists at a depth of 1280 m.

(6) In Cases 2, 3 and $2T$, the total meridional circulation splits into two gyres. There is no overall overturning. When a cold water mass

sinks from the high latitude surface layer, both its temperature and surrounding pressure are increased with depth. Because the compressibility of sea water is decreased with pressure and temperature, the density increase by sinking is somewhat suppressed. In addition, the downward increase of the temperature works to decrease the water density, though the coefficient of thermal expansion is very small at low temperatures. In this way, the high latitude sinking could not readily reach down to the bottom layer. A large single gyre meridional circulation is produced when the water density is calculated from a simple equation of state using a constant coefficient of thermal expansion and ignoring the effect of the pressure and the salinity (for instance, BRYAN and COX, 1967; TAKANO, 1978). In that case, no such processes as mentioned above come into play to weaken the sinking. Then, the model convection is made too strong, which results in overestimate of the meridional overturning.

The primary objective of the present study is to have some insight into the effect of the surface salinity, heat and momentum flux on the general circulation in an ocean in the framework of various simplifications and assumptions. Hence, it is out of the scope to investigate its results in detail in view of the observation in a particular ocean. With these reservations, however, the calculated features are not in agreement with observed features in some respects such as salinity minimum layer missing, convergence of surface currents around 40°～50°N near the eastern boundary.

The computation was done on FACOM 230-75 at the Institute of Physical and Chemical Research. Thanks go to Mr. M. NOGUCHI and the staff of the computer room. Ms S. MATSUYAMA of the Computation Center of the Hôsei University took charge of a part of the programming.

References

BRYAN, K. and M. D. COX (1967): A numerical investigation of the oceanic general circulation. Tellus, **19**, 54-80.

FRIEDRICH, H. and S. LEVITUS (1972): An approximation to the equation of state for sea water, suitable for numerical ocean models. J. Phys. Oceanog., **2**, 514-517.

HELLERMAN, S. (1967): An updated estimate of the wind stress on the world ocean. Mon. Wea. Rev., **65**, 607-626. (correction, 1968, **96**, 63-74).

TAKANO, K. (1978): Effect of the approximation to the equation of state for sea water on the model general circulation. La mer, **16**, 147-161.

塩，熱・塩，熱・塩・風大循環について

高　野　健　三

要旨: 海面での塩分流量による大循環，塩分流量と熱流量とによる大循環，塩分流量と熱流量と運動量流量(風の切線応力)とによる大循環の数値解を示す。海は経度方向には 48°，緯度方向には赤道から 70°N までひろがり，その深さは一定である。格子間隔は 2°，鉛直方向には5層を設ける。これら三つの結果と，塩分が均一な場合の熱大循環――以前に計算ずみ――とからつぎのことがわかる。塩分は大循環を弱めるが，その働きは強くはないので，塩分が変わる場合でも均一な場合でも流速分布には大きなちがいを生じない。しかし，塩分が均一であれば中層の水温は下がる。風の応力は海全体にわたって流速を速め，海全体の平均水温を下げ，表層の平均水温と平均塩分を高め，子午面循環と子午線方向の熱輸送を強める。しかし，子午線方向の塩分流量はほとんど変わらない。駆動力として海面熱流量と塩分流量だけが働く場合には塩分最小層が現われるが，さらに風の応力も加えると塩分最小層は消えてしまう。

学 会 記 事

1. 昭和56年8月31日，東京水産大学において編集委員会が開かれ，La mer 第19巻第4号の編集を行った。

2. 新入会員 （正会員）

氏　名	所　属	紹介者
柳瀬　訓	国土地理院	斎藤　祥

3. 退会者

福尾義昭，飯高季雄，斎藤　祥

4. 会員の住所・所層の変更

氏　名	新住所または新所属
土田武雄	気象庁，統計課
篠田　裕	千葉工業大学
中尾　徹	〒270-11 我孫子市青山台 4-24-5
平良恵仁	〒901-24 沖縄県中城村字南上原葦山原858
井上敏彦	〒363 埼玉県桶川市泉2-19-50, 3-105
森　幹樹	〒320 宇都宮市操町1-21 菅谷方
尾山実美	〒151 渋谷区本町3-21-6 羽田荘5号

5. 交換および寄贈図書

1) 昭和54年度　広島県水産試験場事業報告
2) 研究実用化報告　Vol. 30, No. 6, 7, 8, 9
3) なつしま　No. 53, 54
4) 海洋産業研究資料　Vol. 12, No. 6
5) Publication List 1979（東大 海洋研）
6) 海洋時報　第22号
7) 広島大学生物生産学部紀要　第20巻第1号
8) 新海洋時代に対応する海洋開発関連法制に関する研究
9) 広島日仏協会報　No. 79
10) RESTEC　7号
11) 地盤水理実験施設年報　第6号
12) 鯨研通信　340号
13) 千葉県水産試験場研究報告　第39号
14) JODC ニュース　No. 23
15) 日本プランクトン学会報　第28巻第1号
16) 水産工学研究所報告　第2号
17) 水産工学研究所技報　第2号
18) 航　海　第69号
19) 海洋地質図　No. 16
20) クルーズレポート（地質調査所）　No. 16
21) 海産研ニュース　No. 2
22) Boletim do INIP　1980, No. 4
23) Science et Pêche　N° 307. 308
24) Annales de l'institut océanographique Tome 57
25) Revue des travaux de l'institut des pêches maritimes　Tome XLIII Fasc. 2 et 3, 4
26) Lungfishes, Tetrapods, Paleontology and Plesiomorphy　167-4
27) Bulletin de l'institut de géologie du bassin d'aquitaine　N° 29
28) Rapport annuel　1980
29) 科学通報　Vol. 26, No. 8

6. 本会会員守安実己郎氏は1977年11月から1981年5月までフランス政府給費留学生としてモンペリエ市ラングドック理工科大学理学部に在籍し，1981年7月第3期課程博士課程の学位審査を受け合格した。

日仏海洋学会役員

顧　問　ユベール・ブロッシェ　ジャン・デルサルト　ジャック・ロベール　アレクシス・ドランデール　ベルナール・フランク　ミシェル・ルサージュ　ロベール・ゲルムール　ジャック・マゴー

名誉会長　レオン・ヴァンデルメルシュ

会　長　佐々木忠義

副会長　黒木敏郎，國司秀明

常任幹事　阿部友三郎，有賀祐勝，冨永政英，松生　洽，三浦昭雄

庶務幹事　佐伯和昭

編集幹事　村野正昭

幹　事　石野　誠，井上　実，今村　豊，岩下光男，宇野　寛，川原田　裕，神田献二，菊地真一，草下孝也，斎藤泰一，佐々木幸康，杉浦吉雄，高木和徳，高野健三，高橋　正，辻田時美，奈須敬二，根本敬久，半沢正男，丸茂隆三，森田良美，山中鷹之助　（五十音順）

監　事　久保田　穣，岩崎秀人

評議員　青山恒雄，赤松秀雄，秋山　勉，阿部宗明，阿部友三郎，新崎盛敏，有賀祐勝，石野　誠，石渡直典，市村俊英，井上　実，今村　豊，入江春彦，岩崎秀人，岩下光男，岩田憲幸，宇田道隆，宇野　寛，大内正夫，小倉通男，大村秀雄，岡部史郎，岡見　登，梶浦欣二郎，加藤重一，加納　敬，川合英夫，川上太左英，川村輝良，川原田　裕，神田献二，菊地真一，草下孝也，楠　宏，国司秀明，久保田　穣，黒木敏郎，小泉政美，小林　博，小牧勇蔵，

西条八束，斎藤泰一，斎藤行正，佐伯和昭，
坂本市太郎，　佐々木忠義，　佐々木幸康，
猿橋勝子，柴田恵司，下村敏正，庄司大太郎，
杉浦吉雄，関　文威，多賀信夫，高木和徳，
高野健三，高橋淳雄，高橋　正，谷口　旭，
田村　保，千葉卓夫，辻田時美，寺本俊彦，
鳥羽良明，冨永政英，鳥居鉄也，中井甚二郎，
中野猿人，永田　正，永田　豊，奈須敬二，
奈須紀幸，西沢　敏，根本敬久，野村　正，
半沢正男，半谷高久，樋口明生，菱田耕造，
日比谷　京，平野敏行，深沢文雄，深瀬　茂，
福島久雄，淵　秀隆，増沢譲太郎，増田辰良，
松生　洽，丸茂隆三，三浦昭雄，三宅泰雄，
村野正昭，元田　茂，森川吉郎，森田良美，
森安茂雄，安井　正，柳川三郎，山路　勇，
山中鷹之助，山中一郎，山中　一，吉田多摩夫，
渡辺精一　　（五十音順）
マルセル・ジュグラリス，ジャン・アンクティル，ロジェ・ペリカ

賛　助　会　員

旭化成工業株式会社	東京都千代田区有楽町 1-1-2　三井ビル
株式会社内田老鶴圃新社　内田悟	東京都千代田区九段北 1-2-1　蜂谷ビル
株式会社　オーシャン・エージ社	東京都千代田区神田美土代町 11-2　第1東英ビル
株式会社　大林組	東京都千代田区神田司町 2-3
株式会社オセアノート	東京都世田谷区北沢 1-19-4-202
小樽舶用電機株式会社	小樽市色内町 3-4-3
株式会社オルガノ	東京都文京区本郷 5-5-16
社団法人海洋産業研究会	東京都港区新橋 3-1-10　丸藤ビル
協同低温工業株式会社	東京都千代田区神田佐久間町 1-21　山伝ビル
協和商工株式会社	東京都豊島区目白 4-24-1
小松川化工機株式会社	東京都千代田区岩本町1-10-5　TMMビル5F
小山康三	東京都文京区本駒込 6-15-10　英和印刷社
三信船舶電具株式会社	東京都千代田区神田 1-16-8
三洋水路測量株式会社	東京都港区新橋 5-23-7　三栄ビル
シュナイダー財団極東駐在事務所	東京都港区南青山 2-2-8　DF ビル
昭和電装株式会社	高松市寺井町 1079
新日本気象海洋株式会社	東京都世田谷区玉川 3-14-5
株式会社鶴見精機	横浜市鶴見区鶴見中央 2-2-20
株式会社東京久栄	東京都中央区日本橋 3-1-15　久栄ビル
東京製綱繊維ロープ株式会社	東京都中央区日本橋室町 2-6　江戸ビル
株式会社東邦電探	東京都杉並区宮前 1-8-9
中川防蝕工業株式会社	東京都千代田区神田鍛冶町 2-2-2　東京建物ビル
日本アクアラング株式会社	神奈川県厚木市温水 2229-4
日本テトラポッド株式会社	東京都港区新橋 2-1-13　新橋富士ビル9階
社団法人日本能率協会	東京都港区芝公園 3-1-22　協立ビル
日本プレスコンクリート株式会社	東京都中央区日本橋本石町 1-4
深田サルベージ株式会社	東京都千代田区神田錦町 1-9-1　天理教ビル8階
藤田潔	東京都新宿区四谷 3-9　光明堂ビル　株式会社ビデオプロモーション
藤田峯雄	茨城県北相馬郡藤代町大字毛有 850　株式会社 中村鉄工所
古野電気株式会社	東京都中央区八重洲 4-5　藤和ビル
丸文株式会社	東京都中央区日本橋大伝馬町 2-1-1
三井海洋開発株式会社	東京都千代田区一ツ橋 2-3-1　小学館ビル
宮本悟	東京都中央区かちどき 3-3-5　かちどきビル　㈱本地郷
株式会社ユニオン・エンジニアリング　佐野博持	神戸市中央区海岸通 3-1-1 KCC ビル4F
吉野計器製作所	東京都北区西ケ原 1-14
株式会社離合社	東京都千代田区神田鍛冶町 1-10-4
株式会社渡部計器製作所	東京都文京区向丘 1-7-17

La mer (Bulletin de la Société franco-japonaise d'océanographie)

Tome 19 (1981)

Sommaire

Numéro 1

Numéro 2

うみ(日仏海洋学会誌)

第19巻 (1981 年)

総 目 次

第 1 号

第 2 号

Numéro 3

第 3 号

Numéro 4

日仏海洋学会賞受賞記念講演

第　4　号

Exploiting the Ocean by...

T.S.K.

OCEANOGRAPHIC INSTRUMENTS

REPRESENTATIVE GROUPS OF INSTRUMENTS AND SYSTEMS

T.S-STD MODEL-Ⅰ型

T.S-STD観測装置Ⅰ型は，ケーブル式STDの最新型で音速計及びロゼットサンプラーが，一体構造に組込まれているのを特長とし，各データはリアルタイムで船上記録部のデジタル表示器に表示・デジタルプリンターで印字されると同時に，アナログxy記録計に記録されます。また電子計算機による二次処理を行うための信号が船上記録部から出力されます。

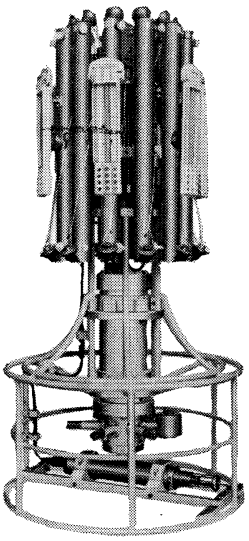

検出部

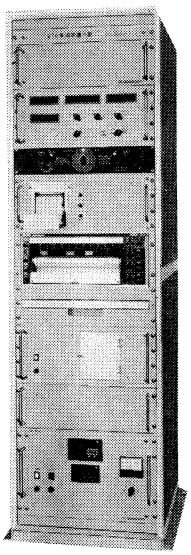

記録部

性　能

	測定範囲	精　度	デジタル表示印字最小桁	計算機用出力
塩　分	31～36‰	±0.03‰	0.01‰	IEEE 488 (GP-IB) BYTE SERIAL 16BIT/WORD
水　温	−2～40°C	±0.05°C	0.01°C	
深　度	0～6,000m	±0.2%FS	1m	
音　速	4,600～5,200ft/s	±1ft/s	1ft/s	

株式会社　鶴　見　精　機

横浜市鶴見区鶴見中央2丁目2番20号　〒230　TEL; 045-521-5252

CABLE ADDRESS; TSURUMISEIKI Yokohama,　TELEX; 3823750 TSKJPN J

OVERSEAS OFFICE; TSK-AMERICA INC. Seattle WASHINGTON

IAWMIYA INSTRUMENTATION LABORATORY

ユニオン・エンジニアリングが
パーフェクトな観測をお約束する

海象・気象計測器

優れた精度・取扱い容易・世界的な実績・豊富な部品在庫・迅速確実なメンテナンス

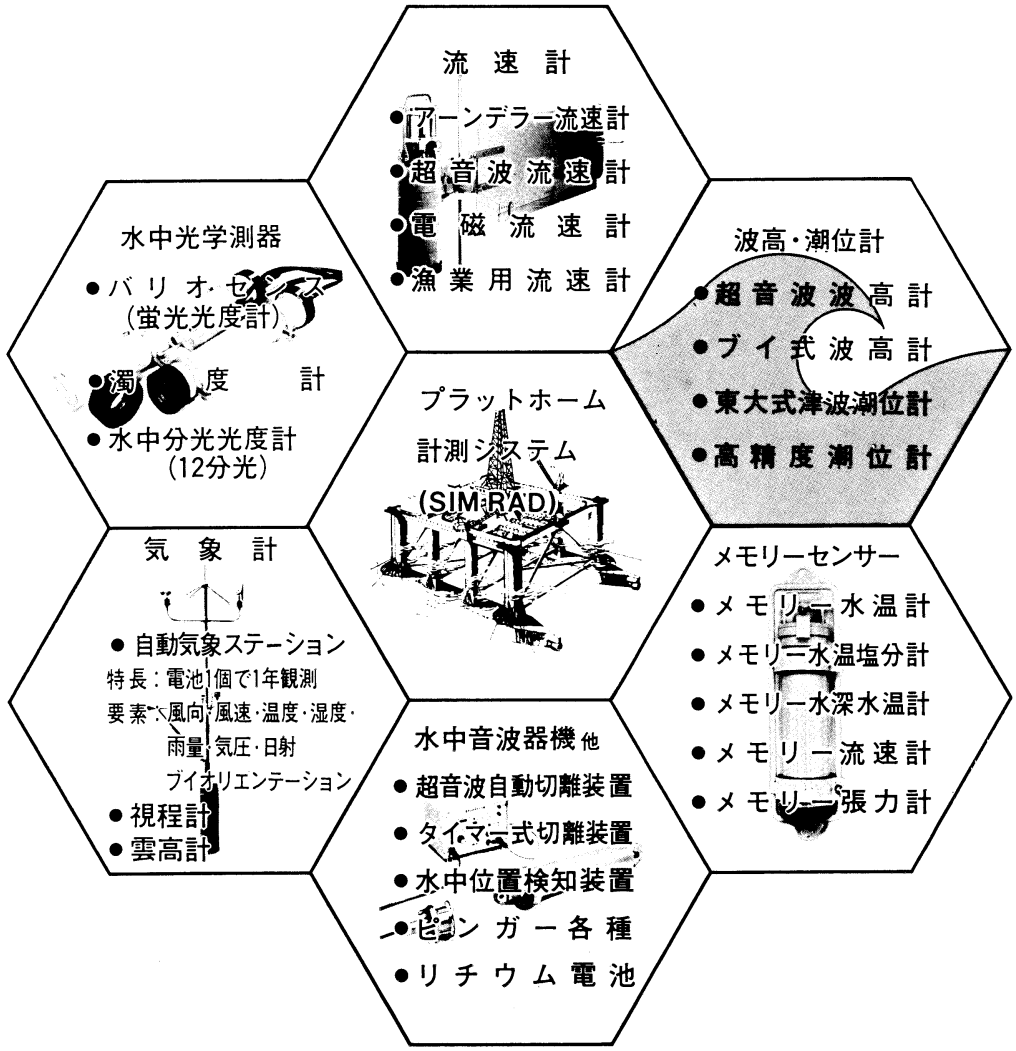

株式会社 ユニオン・エンジニアリング
本　社　神戸市中央区海岸通3丁目1－1
〒650　KCCビル4F　TEL078-332-3381(代)
東京支店　東京都中央区銀座7丁目18
〒104　銀座スカイハイツ602号　TEL03-543-5399

昭和 56 年 11 月 25 日　印刷
昭和 56 年 11 月 28 日　発行

う　み　　第 19 巻 第 4 号

定価 ¥1,200

編集者　冨永政英
発行者　佐々木忠義
発行所　日仏海洋学会
財団法人 日仏会館内
東京都千代田区神田駿河台2-3
郵便番号：101
電話：03(291)1141
振替番号：東京 5-96503

印刷者　小山康三
印刷所　英和印刷社
東京都文京区本駒込 6-15-10
郵便番号：113
電話：03(941)6500

Tome 19　　N° 4

SOMMAIRE

第 19 巻　　第 4 号

目　　次